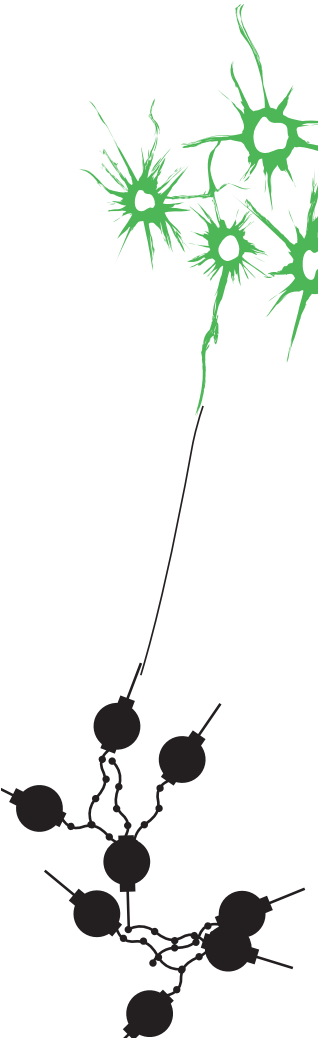

RAM ROBOTICS AND MECHATRONICS

AN INTERACTIVE APPROACH FOR MRI-BASED INTERVENTIONAL NAVIGATION

I. (Idse) Kuijper

MSC ASSIGNMENT

Committee:
prof. dr. ir. S. Stramigioli
dr. ir. K. Niu
dr. ir. W.M. Brink
dr. V. Groenhuis, MSc
dr. J. Dasdemir

October, 2024

071RaM2024
Robotics and Mechatronics
EEMCS
University of Twente
P.O. Box 217
7500 AE Enschede
The Netherlands

UNIVERSITY OF TWENTE. | TECHMED CENTRE UNIVERSITY OF TWENTE. | DIGITAL SOCIETY INSTITUTE

An Interactive Approach to MRI-based Interventional Navigation

Idse Kuijper[1], dr. Vincent Groenhuis[1], Wyger M. Brink[2], prof. dr. ir. Stefano Stramigioli[1], dr. ir. Kenan Niu[1]

***Abstract*— Magnetic resonance imaging (MRI) offers higher sensitivity in detecting invasive breast cancer, enabling the identification of lesions at earlier, more treatable stages. However, unlike ultrasound-guided biopsies, current MRI-guided biopsies lack real-time confirmation of lesion removal, necessitating multiple verification scans and follow-up MRI's. Recent advanvements in real-time MRI imaging, with interactive imaging of a slice at up to 30Hz, present opportunities for MRI-safe manipulators by enabling closed-loop control through intra-operative imaging.**

This study proposes a methodology for closing the loop for the Sunram 7 pneumatically actuated breast biopsy robot using MR image feedback in-plane of the end-effector. By leveraging the segmented tip and base position with the planned needle path, an improved estimate of the needle's position and orientaiton is achieved, potentially enhancing target accuracy. Features, such as automatic calibration between image frame and robot base frame, multi-planar reconstruction, path planning, and discretization optimization, provide essential support in the biopsy procedure.

Proof-of-concept validation within the MRI-environment demonstrated a significant reduction in the mean euclidian position error, from 8.81 mm using sole feed-forward estimation to 1.11 mm with the proposed methodology, highlighting its potential to improve the targeting accuracy of the robot. The proposed methodology is novel in the fact that it automatically calibrates the robot based on the new estimation for direct control of the planned path.

In conclusion, this methodology shows promising results in improving the positional accuracy of the Sunram 7 robot's end-effector and warrants further validation for definitive implementation.

I. INTRODUCTION

Breast cancer is the leading cancer in terms of incidence and death among females worldwide, accumulating to 2,308.897 new cases and 665.684 deaths in 2022 [1, 2]. Affecting about one in ten women living in western countries during their lifetime [3], and showing significant increase for high-risk women with an inherited predisposition that can give rise to an early onset of the disease, giving a lifetime risk greater than 50-60% [3]. The 5-year relative survival rate of breast cancer in the United States is shown to be 91%, with a significant increase to 99% when the tumor is diagnosed at a local stage [4]. Indicating the importance of early detection and screening of malignant lesions.

[1] Robotics and Mechatronics, University of Twente, Enschede, 7500AE, The Netherlands i.kuijper@student.utwente.nl (I.K.), k.niu@utwente.nl (K.N.), v.groenhuis@utwente.nl (V.G.), s.stramigioli@utwente.nl (S.S.)

[2]Magnetic Detection and Imaging group, TechMed Centre, University of Twente, Enschede, 7500AE, The Netherlands w.m.brink@utwente.nl (W.B.)

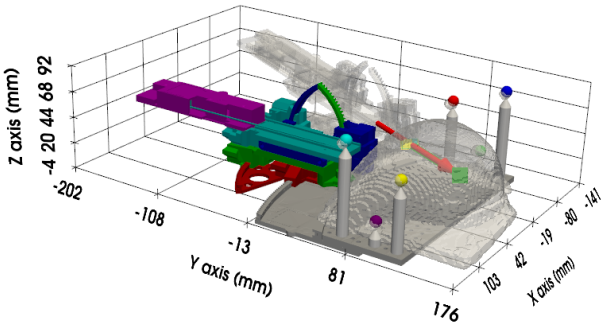

Fig. 1: Virtual surrogate of the Sunram 7 robot with the base plate, six MRI identifiable markers and the mapped breast phantom mesh. The virtual surrogate of the Sunram 7 is in the zero position and the greyed-out version indicates the planned configuration at the point of entry.

Current screening recommendation differs between average-risk females and high-risk females; average-risk females can rely on annual or biennial mammography screening from age 40 onwards whilst high-risk females should rely on earlier mammography screening adjunct to annual Magnetic Resonance Imaging (MRI) screening [5, 6]. MRI's higher sensitivity to invasive breast cancer indicate its ability to detect it at a more favorable stage as opposed to other imaging methods [7, 8]. Even shown in research to have detected all 14 Ductal Carcinoma In Situ's (DCISs), compared to mammography and ultrasound each detecting five DCISs [9]. Still due to high cost, long screening time and debatable specificity of MRI this imaging method is recommended only for women in the high-risk group or for situations where the primary breast cancer is too small for detection using mammography or ultrasound (US) [8, 9]. To address the low specificity of MRI it is recommended to perform a targeted US upon identification of lesions suspicious for malignancy during MRI screening, referred to as a 'second-look US' [7]. This way the practitioner can confirm the tissue is indeed malignant and perform an US guided biopsy to establish diagnosis. The presence of an US correlate, however, is only reported in 23-71% of cases and occlusion of the corresponding abnormality indicate an MRI-guided biopsy is the only viable option for diagnosis [10, 11]. Obtaining tissue diagnosis is especially imperative for MRI-detected abnormalities because of similar appearance of benign and malignant lesions on MRI [12].

Presently, the MRI-guided biopsy procedure is complicated, lengthy and an imperfect procedure, requiring a mul-

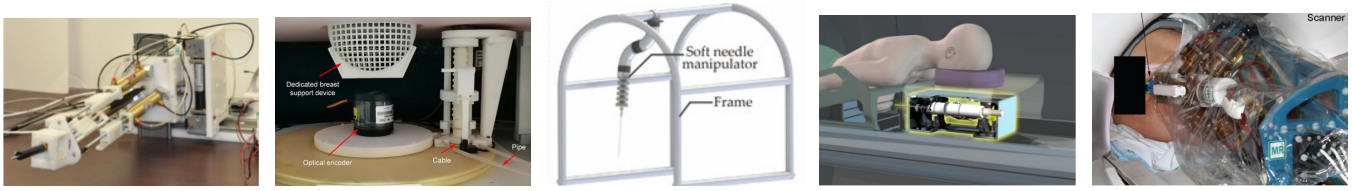

(a) B. Yang et al. [13] (b) C. Song et al. [14] (c) J. Cheng et al. [15] (d) M. Amvari et al. [16] (e) D. Stoianovici et al. [17]

Fig. 2: Various MRI-compatible biopsy robots for either the breast or prostate.

titude of scans and samples to be taken [7, 10]. Upon start of the breast biopsy procedure the patient is positioned in prone position on the examination table and the patient's breast is compressed in a grid-like square that doubles as localization device. Immobilisation of the breast is a prerequisite for accurate sampling as it allows for better elimination of artefacts or blurring from respiratory motion and reduces movement of the breast tissue during insertion [7]. A pre-contrast MRI sequence is obtained to initialize the fiducials in the localization device to allow for mapping between localization device and image space. This is followed by a dynamic MRI sequence combined with administration of contrast medium (gadolinium-based agent) into the breast [10]. Depending on lesion kinetics, a single or two imaging sequences after contrast agent administration are usually sufficient for lesion identification [10] with other centers performing five sequences [7]. These scans allow for selection of the lesion and entrance site in image space. Using the previously obtained mapping, the target point can be transformed into an entrance position and depth on the localization device for biopsy positioning [10]. The entrance site of the breast is prepared for insertion by cleaning and administration of local anesthesia. A coaxial system consisting of plastic inducer with numeric gradation and an introductory metallic stylet is then used and advanced into the breast upto the indicated depth at the calculated site of entry. The stylet is swapped with a blunt-tipped MRI-negative plastic MRI introducer and a MRI sequence is obtained to verify the position of the MRI introducer in relation to the area to be biopsied. If needed, the needle position is adjusted and confirmation scans are performed, repeating the cycle until adequate biopsy position is obtained. Upon obtaining adequate positioning, the vacuum assisted biopsy (VAB) needle can be placed and appropriate samples taken. Finally, a localization marker clip is deployed labelling the site of biopsy and a final MRI sequence is performed to verify that the correct tissue has been sampled and ensuring clip position.

The successful execution of MRI-guided vacuum-assisted biopsies (VAB) is prone to human errors and relies heavily on the extensive training and experience of the healthcare team. The National Health Service Breast Screening Programme recommends that these procedures be performed by breast centres conducting a minimum of 12 MRI-guided biopsies and at least 50 image-guided VABs anually [7]. VAB is considered advantageous over core needle biopsy due to its ability to extract larger volumes of tissue as opposed to core needle biopsy, reducing sampling errors [18]. Sample size typically ranges from 40 to 310mg depending on needle gauge (14G to 8G), compared to 17mg from core needle biopsies [18]. Additionally, research indicates the collection of 4 to 24 samples dependent on exact gauge size and lesion dimensions [7, 10], further enhancing the likelihood of obtaining sufficient material for accurate diagnosis. However, the increased volume of tissue sampling can lead to unnecessary removal of healthy tissue, raising concerns regarding patient comfort and potentially unnecessary breast damage.

Moreover, the grid-like orientation device limits the angle of entry and the need for accessibility of the patient by the practioner necessitates movement of the patient in and out of the MRI bore, complicating the workflow. Unlike US-guided biopsy, current MRI-guided VAB lacks real-time confirmation of lesion removal, necessitating multiple verification scans during the procedure and follow-up MRIs to ensure complete removal, especially when benign histopathology results are obtained [19]. Challenges posed by the gadolinium based contrast agents (GBCA) washing out during procedure and post-biopsy changes including air, hemorrhage, and local anesthesia further complicate assessment of these verification scans [12, 19].

The limitations of the manual MRI-guided procedure in combination with current development of real-time MRI imaging providing interactive imaging of a slice at up to 30Hz [20] provides opportunities for MRI-safe manipulators to fill the gaps in the current procedure through use of intra-operative imaging. The benefits of the integration of MR-safe robotic manipulators into medical applications has been shown to include higher accuracy and precision, standardization of the procedure, stability, and less insertions, realizing procedures that are faster, less expensive and produce less patient trauma [21]. The use of real-time MRI imaging is not an entirely novel idea, B. Yang et al. presents a six degree of freedom (DOF) teleoperated primary-secondary MRI-compatible robot placing a guiding cannula for needle insertion in the breast under 2.5 frames per second MRI guidance [13]. Showing that the secondary robot could operate under continuous MRI with no visually-detectable image distortion and minimal loss in signal to noise ratio (SNR), but with mild field homogenity distortion. This robot, however, is not autonomous and places only a guiding cannola in the breast, leaving the diagnostic procedure to be performed manually, thereby limiting its improvement in

terms of amount of scans and patient movement in and out of the MRI-bore. Another MR-compatible robot using real-time feedback during navigation is presented by C. Song et al [14]. This, however, makes use of a stereo camera setup detecting three personalized markers reconstructing the 14G considered rigid needle upon insertion. This system also relies on manual insertion of the biopsy needle through the needle guide. The pneumatically actuated soft needle manipulator, called SoNIM, presented by J. Cheng et al. has also shown to achieve needle manipulation in the MR environment using a motion capture system [15]. Demonstrating the potential of the SoNIM to perform needle manipulation in minimally invasive surgeries, but mentioning the need for closed-loop control in an MR environment through either fiber Bragg grating (FBG) sensors or processing of 3D MRI data in real-time. It does demonstrate the possibility of using MRI as an alternative way to measure the configuration of the SoNIM to achieve closed-loop control, but is yet to implement it. For breast biopsies also the MR-compatible image guided automated robot presented by M. Amvari et al. demonstrates sub-millimeter accuracy and repeatability [16]. However, this system lacks any real-time image guidance as the patient is moved out of the MRI bore for needle insertion due to significant artifacts produced by the commercially available biopsy tools used. For prostate biopsy D. Stoianovici et al. proposed a FDA approved MR-safe robot called MrBot consisting of a MR-safe 6 DOF parallel link structure mounted on the MRI table [17]. This system positions a needle-guide to the target position without any continuous MRI and relies on manual biospy.

This research aims to **close the loop for MRI-guided biopsy procedures through an interactive approach to real-time MRI-based interventional navigation**. The findings are presented according to the following structure. Section II, methodology, will provide a comprehensive description of the proposed system, including details on the robot design, kinematics, calibration between image and robot space, path-planning, discretization error minimization, feedback loop, and proposed experimental validations. Following this, the thesis will present the results of the experimental validations. These results are synthesized and highlighted in significance in the conclusion. Finally, the discussion will analyze the findings, compare these to the state of the art and discuss their implications for future MRI-guided biopsy practices.

II. METHODS

Achieving closed-loop control in MRI-guided biopsy procedures requires the seamless integration of various components. This research specifically addresses closing the control loop for the Sunram 7 biopsy robot [22], whilst performing biopsies on PVC-P-based breast phantoms within a 1.5T MRI scanner (SIEMENS 1.5T MAGNETOM Aera, Siemens Healthineers, Erlangen, Germany). A high-level overview of the system architecture and its key components is provided in Fig. 3, outlining the envisioned setup for this study.

A. System Overview

Several components of the envisioned MRI-guided biopsy system were adopted from pre-existing designs and remained unchanged. These include the MRI scanner (SIEMENS 1.5T MAGNETOM Aera, Siemens Healthineers, Erlangen, Germany), Siemens Access-I Application Programming Interface (API, Siemens Healthcare GmbH), the mechanical design of the Sunram 7 biopsy robot, and its pneumatic controller board [22]. The study focuses on the needed components and algorithms for closing the control loop and integrating real-time feedback as shown in Fig. 3 whilst maintaining these established system components. Throughout this paper four coordinate frames and a configuration space can be identified:

1) **Dicom Volume Coordinate System (DCS):** The coordinate frame obtained when loading a three dimensional MR imaging sequence, with the origin located at the top-left of the first slice.
2) **Robot Base Frame (RBF):** The coordinate frame with its origin aligned with the robot base as indicated in Fig. 4.
3) **Patient Coordinate System (PCS):** The coordinate frame with its origin at the isocentre of the MRI scanner.
4) **Image Coordinate System (ICS):** The two dimensional coordinate frame of singular MRI slices with its origin in the top-left.
5) **Joint Space of the Robot (Q):** The space representing the internal state of the robot joints, defined by the set of joint angles and position that describe the configuration of the Sunram 7.

Furthermore, the envisioned procedure can be split up into three phases: pre-operative, intra-operative and post-operative.

The pre-operative phase focuses on establishing calibration between the dicom volume coordinate system and the robot space. This relies on identifying six MRI-visible markers within the field-of-view (FOV) of the three-dimensional calibration scan. The position of these markers in RBF are known, and using image processing these six markers are identified in the DCS. A Procrustes analysis can be performed on the coordinates of these six identifiable markers in both frames providing the estimated transformation between both frames [23]. Once the transformation is obtained, the clinician can select the target for biopsy using multi-planar reconstruction (MPR) of the DICOM images, which can then be transformed to the RBF. Subsequently, the clinician selects the desired angle of approach in robot base frame and uses the inverse kinematics (IK) mapping of the Sunram 7 to obtain the required position of the Sunram 7 in joint space. Using the required orientation and target position, the point of entry into the breast phantom is also identified by placing its outside mesh in the RBF and finding the point of intersection. Using both of these identified points; target and entry, in joint space, the robots path can be planned. Movement is performed up until the needle touches the breast

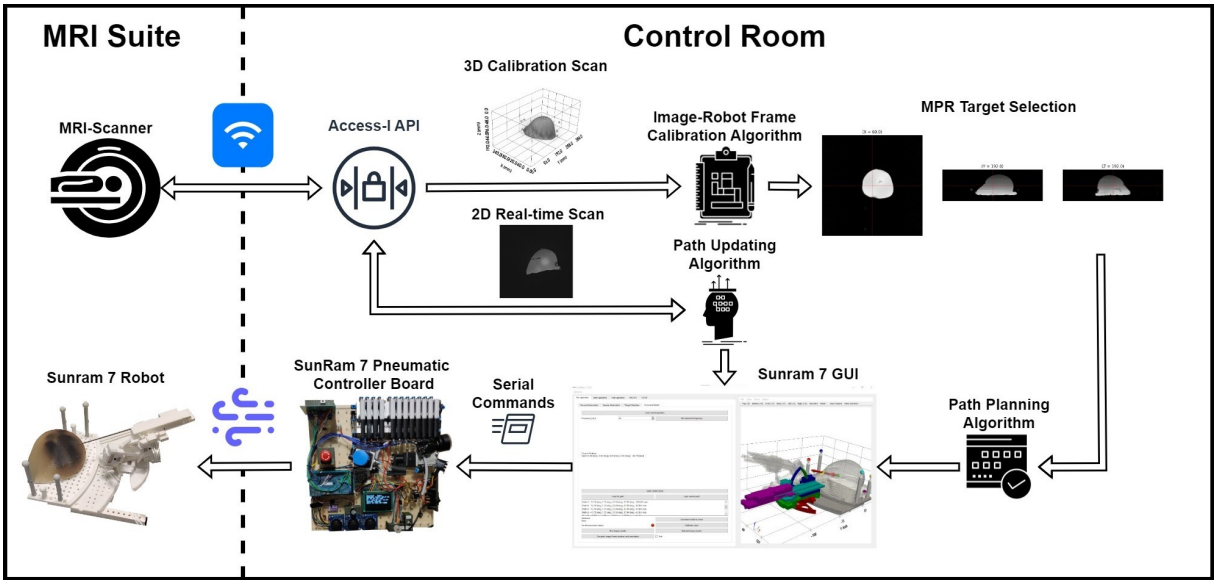

Fig. 3: The proposed system to close the control loop of the Sunram 7 robot. The Siemens Access-I API is used for two-way communication over the local area network between MRI-scanner and the system. Upon initialization, a full three-dimensional scan including six fiducial markers is used to map image space to robot space as to be able to identify the target position relative to the robot. Based on the Sunram 7's inverse kinematics the needed path is generated to reach this target. This is sent to the Sunram 7 pneumatic controller as serial commands in order to move the Sunram 7 along the chosen path using the pneumatic stepper motors. Meanwhile, real-time imaging is obtained using MR images by scanning an oblique slice of the planned needle tip position and orientation. These images showing the needle and target provide feedback on the movement of the Sunram 7, thereby closing the control loop.

in the pre-operative phase.

The intra-operative phase is where the real-time feedback loop is engaged. The needle is inserted into the breast phantom up to 10 mm, allowing for initial needle recognition using the YOLOV8 segmentation described in Z.J. Tai et al. [24]. The inner-workings of the segmentation methodology is outside the scope of this research and implementation is based on the findings described in Z.J. Tai et al. [24]. As a starting point for segmentation of the needle, its position and orientation in PCS are required. The needle position and orientation can be obtained by mapping the joint position using the forward kinematics. This position and orientation in RBF can be converted to PCS by: (1) mapping it to DCS using the inverse transformation matrix obtained by Procrustes analysis and (2) mapping between DCS and PCS obtained from the scanning metadata. The Access-I API used for communication between MRI scanner and application uses the PCS for selecting a slice position and orientation. Using the obtained slices at needle tip position, the segmentation algorithm tracks the needle throughout the procedure and provides the system with the coordinates of the needle tip, the needle base in ICS. The obtained needle tip position and orientation are used in combination with the planned path to obtain a new estimated position of the needle through Kalman filtering. Based on the newly estimated position the planned trajectory can be adjusted to compensate for any errors in positioning of the pneumatic stepper motors [22]. This phase ends with firing the biospy needle and retracting it until outside of the breast phantom.

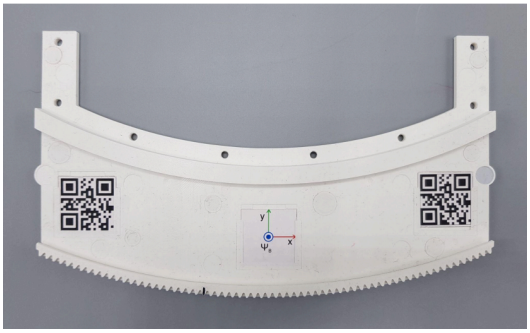

Fig. 4: The origin of the robot base frame indicated on the base plate of the Sunram 7, the serrated edge on the bottom are the teeth for joint 1 [25].

The post-operative phase consists of releasing the needle, acquiring the biopt and resetting the Sunram to its zero position for next use.

B. Sunram 7 robot modelling and kinematics

As stated, this research aims to close the control loop for the Sunram 7 robot developed at University Twente and presented by H. Ranjan et al. [22]. The Sunram 7 is the fully 3-D printed five degrees of freedom pneumatically actuated robot depicted in Fig. 5. The only non-MRI-safe component is the needle, which is an off-the shelf, non-magnetic MR-conditional titanium biopsy needle sized 14

gauge (⌀2.1 mm) and mechanically modified to fit in Sunram 7's pneumatic biopsy gun [22]. This system has the benefit that it is MR safe, meaning that it can be positioned close to the magnet's isocenter and continuous MRI scanning is possible even when in motion [22]. The robot is equipped with five joints, comprising of four revolute joints ($J1$ to $J4$) and one prismatic joint ($J5$), which enable the robot to target spatially defined lesions from various azimuth and elevation angles.

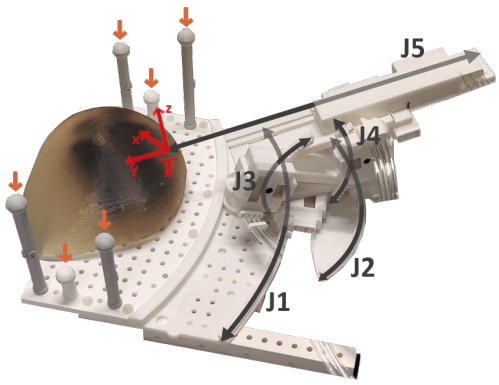

Fig. 5: The Sunram 7 robot annotated with its joint directions (gray) displayed together with its base, the six MRI identifiable markers (orange), a breast phantom and the tool frame T (red).

1) Forward Kinematics: The position and orientation of the needle tip is defined by the manipulator kinematics of the Sunram 7, more specifically its five joints. This mapping of the tool frame T relative to the base frame S based on the joint positions is represented by the forward kinematics $g_{st} : Q \to SE(3)$ [26]. To describe this mapping the base frame S is considered to coincide with the RBF, and all connections between the serial chain joints of the Sunram 7 as depicted in Fig. 5 are considered to be rigid. The joint space, $Q = (\theta_1, \theta_2, \theta_3, \theta_4, \theta_5)$, of the Sunram 7 consists of all possible values for the joints of which the limits are indicated in table I. The general formula for the forward kinematics map of an open-chain manipulator, as the Sunram 7 is, can be described by [26]:

$$g_{st}(\theta) = e^{\hat{\xi}_1\theta_1} e^{\hat{\xi}_2\theta_2} \dots e^{\hat{\xi}_n\theta_n} g_{st}(0), \tag{1}$$

where n is the number of joints, ξ_i's are the twists numbered sequentially starting from the base. The twist of a revolute joint has the following form [26]:

$$\xi_i = \begin{bmatrix} -\omega_i \times q_i \\ \omega_i \end{bmatrix}, \tag{2}$$

where $\omega_i \in \mathbb{R}^3$ is a unit vector in the direction of the twist axis and $q_i \in \mathbb{R}^3$ is any point on the axis. For a prismatic joint [26]:

$$\xi_i = \begin{bmatrix} v_i \\ 0 \end{bmatrix} \tag{3}$$

where $v_i \in \mathbb{R}^3$ is a unit vector pointing in the direction of translation. All of these vectors and points are specified for the Sunram 7 relative to the RBF in table I.

The exponential of the twist, considered as $\xi_i = \begin{bmatrix} \mathbf{v} & \omega \end{bmatrix}^T$, is calculated as follows:

$$e^{\hat{\xi}\theta} = \begin{bmatrix} e^{\hat{\omega}\theta} & (I - e^{\hat{\omega}\theta})(\omega \times \mathbf{v}) \\ \mathbf{0} & 1 \end{bmatrix}, \tag{4}$$

where for $\omega = \begin{bmatrix} \omega_1 & \omega_2 & \omega_3 \end{bmatrix}^T$:

$$\hat{\omega} = \begin{bmatrix} 0 & -\omega_3 & \omega_2 \\ \omega_3 & 0 & -\omega_1 \\ -\omega_2 & \omega_1 & 0 \end{bmatrix}. \tag{5}$$

The exponential is then defined as follows:

$$e^{\hat{\omega}\theta} = I + \hat{\omega}\sin\theta + \hat{\omega}^2(1 - \cos\theta). \tag{6}$$

Using these definitions, the only requirement left for completing the forward kinematics map $g_{st}(\theta)$ of the Sunram 7 is the transformation matrix from base frame S to tool frame T (Fig. 5) at zero position $Q(\mathbf{0})$, which is constructed as follows:

$$g_{st}(\mathbf{0}) = \begin{bmatrix} I_{3\times3} & \mathbf{p}_{EE} \\ 0_{1\times3} & 1 \end{bmatrix}, \tag{7}$$

where $\mathbf{P}_{EE} = \begin{bmatrix} 13.5 & 127 & 41.0 \end{bmatrix}^T$.

2) Inverse Kinematics: Obtaining the required joint positions for the Sunram 7 end-effector to be at a certain position and orientation is done through the inverse kinematics map of the system. This is a non-trivial procedure, but by exploiting the specific kinematic configuration of the Sunram 7; (1) the projection of the line along the end-effector in the XY-plane solely depends on J1 and J2, (2) the Z-component of the end-effector orientation solely depends on J3 and J4, and (3) J5 is a pure translation along the orientation axis, the procedure can be separated into the following three respective steps.

J1 and J2 are dependent solely on the end-effector projection in the XY-plane. Thus, a projection, $\hat{\mathbf{l}}(\lambda) = \hat{\mathbf{p}}_0 + \lambda\hat{\mathbf{d}}$, of the line along the end-effector, $\mathbf{l} = \mathbf{p}_0 + \lambda\mathbf{d}$, onto the XY-plane is used, as depicted in Fig. 6. Note that the end-effector is offset with 13.5 mm and 15 mm in the x- and z-direction respectively compared to its joints in the end-effector frame. To compensate for these displacements the following line parallel to the end-effector is used for step one and two in the analysis:

$$\hat{\mathbf{p}}_0 = \mathbf{p}_0 + R_{EE} \begin{bmatrix} -13.5 \\ 0 \\ -15 \end{bmatrix} \tag{8}$$

where R_{EE} is the rotation matrix that transforms the orientation of the end-effector in zero coniguration (unit vector in the +y-direction) to the required orientation of the end-effector. One can find the projection line simply by taking only the x- and y-component of both the position vector $\hat{\mathbf{p}}_0$ and the orientation of the end-effector $\mathbf{d}$. One constructs a helper circle in the XY-plane of all possible

TABLE I: Information on the joints of the Sunram relevant to the forward kinematics of the system.

Joint	Type (unit)	Limits	Direction $\hat{\mathbf{d}}$	Position $\mathbf{p}$	Stepsize
1	revolute (°)	$[-20, 20]$	$\omega_1 = \begin{bmatrix}0 & 0 & 1\end{bmatrix}^T$	$q_1 = \begin{bmatrix}0 & 240 & 0\end{bmatrix}^T$	0.13
2	revolute (°)	$[-40, 40]$	$\omega_2 = \begin{bmatrix}0 & 0 & 1\end{bmatrix}^T$	$q_2 = \begin{bmatrix}0 & 12 & 0\end{bmatrix}^T$	0.38
3	revolute (°)	$[0, 50]$	$\omega_3 = \begin{bmatrix}1 & 0 & 0\end{bmatrix}^T$	$q_3 = \begin{bmatrix}0 & -58 & 26\end{bmatrix}^T$	0.58
4	revolute (°)	$[0, 50]$	$\omega_4 = \begin{bmatrix}-1 & 0 & 0\end{bmatrix}^T$	$q_4 = \begin{bmatrix}0 & 2 & 26\end{bmatrix}^T$	0.58
5	prismatic (mm)	$[-120, 15]$	$v_i = \begin{bmatrix}0 & 1 & 0\end{bmatrix}^T$	n.a.	0.60

locations for the axis of J2, this is represented by a circle centered around the axis of J1 position with a radius of 228 mm. The intersection points of the projected line with this circle, and the center of J1 provide the necessary information to obtain the configuration of J1 and J2. J1 is equal to the angle between the line from the origin to the centre of J1 and the line from the centre of J1 and the intersection of the projection line in the 180° on the side of the Sunram 7. J2 is equal to the angle between the latter and the projection line.

A similar procedure can be used to obtain J3 and J4 with its geometry presented in Fig. 7. Now with the added caveat that the plane in which these joints move is dependent on J1 and J2. In order to obtain the position of the plane that encompasses these joints the forward kinematics are used to obtain the position of the axis of J3, similar to what is described in eq. (1):

$$\mathbf{p}_3(\theta) = e^{\hat{\xi}_1\theta_1} e^{\hat{\xi}_2\theta_2} q_3, \tag{9}$$

with q_3 in homogeneous coordinates. A circle positioned along the end-effector is constructed around the found position of the axis of J3, $\mathbf{p}_3$, with a radius equal to 60 mm, providing all possible positions of the axis of J4. Positioning the circle along the end-effector is achieved by coinciding it with the plane at the position of the axis of J3, $\mathbf{p}_3$, with a normal vector equal to the cross product of the orientation vector indicated in eq. (8) and the unit vector $\begin{bmatrix}0 & 0 & 1\end{bmatrix}^T$. J3 can be found as the angle between the orientation vector projected onto the XY-plane and the line between the position of J3 and the intersection with the circle with the largest Y-value. J4 is equal to the angle between the latter line and the orientation line indicated in eq. (8).

Knowing J1-4, the position of J5 can be obtained by filling in eq. (1) with J5 equal to zero. The obtained position of the end-effector can be compared with the required position of the end-effector, and the distance between these points is the required value for J5.

3) Workspace: The Sunram 7 has a reachable workspace of 4.1L [22]. It, however, cannot reach all of the points inside this volume at an arbitrary insertion angle. To get an idea of the versatility of the Sunram 7 throughout the volume the workspace is analyzed using two methods:

1) **Monte Carlo method:** random sampling [27].
2) **Inverse Kinematics method:** variation of orientations a voxel in the volume can be reached with.

The Monte Carlo method is done by sampling 100.000 random joint configurations within the Sunram 7 joint limits depicted in Table I and computing the associated end-effector positions and orientations using the forwards kinematics

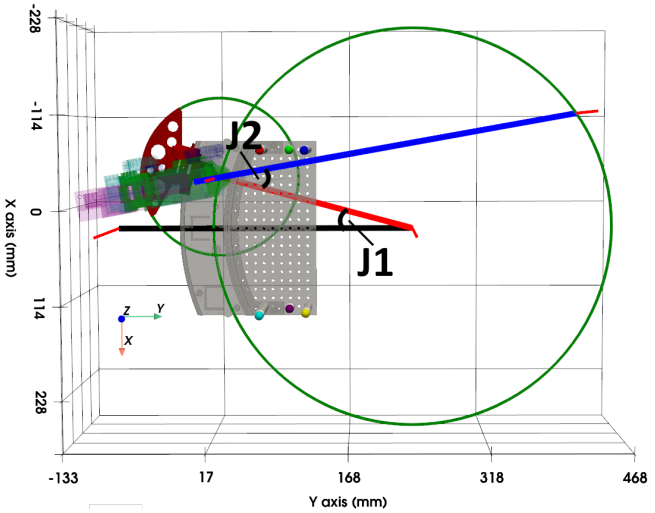

(a) Top view

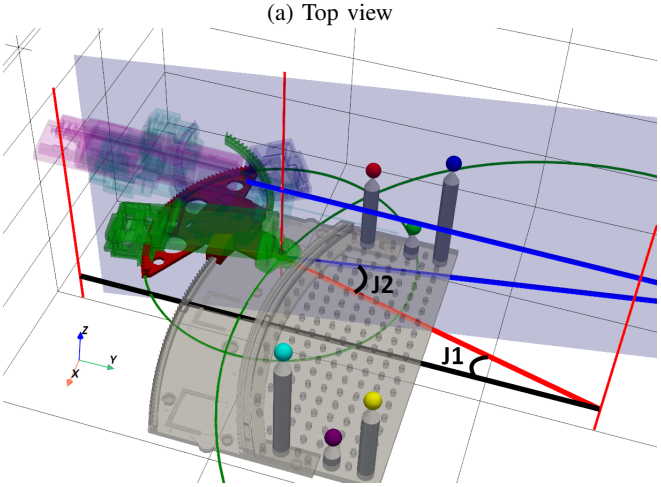

(b) Isometric view

Fig. 6: Geometric relation between Sunram 7 configuration and joint 1 and 2 depicted in RBF. The large green circle is centered around the axis of J1 with the radius equal to the distance of the axis of J2 from the axis of J1. Indicating all possible positions of the axis of J2. The smaller green circle represents J2. The blue lines are the line along the end-effector and its projection on the XY-plane. The black line is the line through the axes J1 and J2 at zero configuration. Associated with the plots is a depiction of the orientatation of the RBF coordinate frame axes.

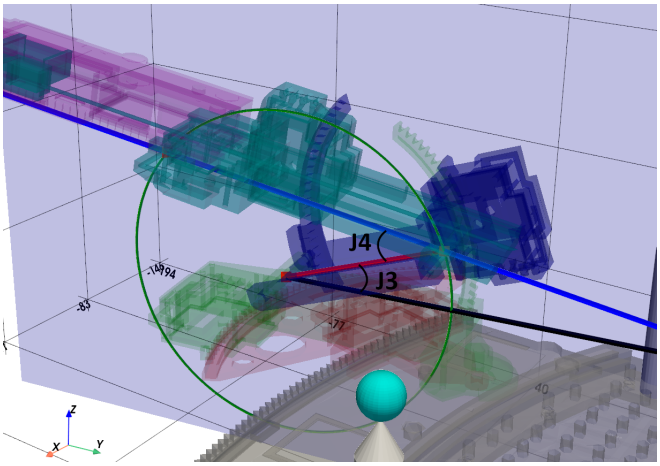

Fig. 7: Geometric relation between Sunram 7 configuration and joint 3 and 4. The green circle is centered around J3 with the radius equal to the distance of the center of J4 from J1. The blue line is the line along the end-effector, adjusted with the offset. The black line is the projection of the blue line onto the XY-plane at the height of the centre of J3.

mapping. The obtained workspace is divided into isotropic voxels of length 10 mm, and for each voxel within the workspace a simple statistical analysis is performed on the acquired end-effector orientation vectors for the end-effector positions inside the voxel. The variation in orientation with which the Sunram 7 is able to reach these voxels is given a quality factor based on the spread in these orientation vectors. The angle each orientation vector makes with the mean orientation vector in the respective voxel is calculated:

$$\cos\theta_i = \frac{\mathbf{v_i} \cdot \mathbf{v}_m}{|\mathbf{v}_i||\mathbf{v}_m|} \tag{10}$$

where θ_i is the angle the i-th orientation vector $\mathbf{v}_i$ makes with the mean orientation vector in that voxel $\mathbf{v}_m$. The standard deviation of this spread in angles is used as the quality factor of each voxel, an indicative measure of the versatility of the end-effector orientation at that position.

The Monte Carlo result, however, does not result in an equal amount of tests throughout the workspace volume. Therefore, the inverse kinematics method relies on creating 100 equally spaced orientation vectors in a cone of 90° around the positive y-direction. For each voxel within the workspace obtained by the Monte Carlo method, the inverse kinematics is performed for all 100 vectors and the amount of orientation vectors that can be reached at each voxel are counted. Then a quality map is made based on the normalized amount of orientations that can be reached out of these 100 vectors for each of the voxels in the workspace.

C. System Calibration

A prerequisite for planning the trajectory of the Sunram 7 is the relative position of the target in the breast phantom with respect to the robot base. The methodology used for obtaining this mapping is an adapted version of the Procrustes method presented in L. Marx et al. [28], by calculating the required translation, scale and rotation to aquire the best match between the identified positions in DCS and the known position of the six markers in RBF.

1) Image Processing: Before the Procrustes analysis can be performed the six markers should be identified in the DCS. After applying a Gaussian filter, the obtained dataset is separated into background noise and tissue/markers using a threshold value obtained by Otsu's method [29]. Separating the breast phantom tissue from markers is done using a Fast Fourier Transform (FFT) template matching algorithm [30]. The template is constructed based on the known dimensions of the markers and the voxel size of the MRI scan. Specifically, an isotropic cubic template with side length equal to the marker diameter (∅10 mm) plus a padding margin of 3 mm is employed. At the center of the template, a spherical region with a diameter equal to that of the markers (∅10 mm) is set to a value of 1, representing the marker region. The surrounding padding margin is assigned a value of -1 to penalize the correlation factor when background is matched with tissue in the MRI image. An exhaustive search throughout the volume using this template provides the correlation factor for each voxel. Applying a threshold to the result identifies which voxels can be considered part of a marker. All connected voxels above this threshold are then grouped and considered part of the same marker. Subsequently, the estimated position of each of the detected markers is taken as the centroid of their respective group. Once the position of each of the separate markers is obtained, the one requirement left is to match each marker in DCS to their respective ground truth. This is done using a Python adaption of the closest pair correspondence algorithm presented in L. Marx et al. [28].

2) Procrustes Analysis: Upon obtaining the two sets of linked positions, one in DCS and the ground truth in RBF, the Procrustes analysis is used to obtain a transformation matrix that maps the image frame best to the ground truth according to the following least-squares criterion [23]:

$$S_{12} = \min||TA_{DCS} - A_{RBF}||^2, \tag{11}$$

where X_{DCS} and X_{RBF} are the sets of linked marker positions in image frame and ground truth respectively, and T is the obtained transformation matrix. This procedure starts by centering each set around the origin by subtracting the centroid of the sets of points from their respective matrix. Followingly, the scale factor can be obtained using the ratio of the Frobenius norms of both matrices [28]:

$$s = \frac{||A_{RBF}||_F}{||A_{DCS}||_F} \tag{12}$$

with s the scale factor, $||A_{RBF}||_F$ and $||A_{DCS}||_F$ the Frobenius norm of the ground truth positions and the image positions respectively. The Frobenius norm is defined as:

$$||A||_F = \sqrt{\sum_{i=1}^{n}\sum_{j=1}^{3}|a_{ij}|^2}, \tag{13}$$

where n is the number of points and j each coordinate of the point. By scaling the centered set of points in the image frame using this scale factor, the magnitude between ground truth and image frame are aligned. Finally, the required rotation from DCS to RBF can be obtained using Singular Value Decomposition (SVD). The SVD states that a matrix **A** can be separated into unitary rotation matrices and the 'stretching'-factors or singular values as follows [31]:

$$A = U\Sigma V', \tag{14}$$

Where U and V' are unitary matrices holding the vector directions and Σ is the diagonal matrix containing singular values of matrix A. Taking the SVD of the cross covariance matrix between image and ground truth $A_{DCS}A'_{RBF}$, where the positions in image frame are scaled and centered and the positions in ground truth are centered, we get the optimal Procrustes rotation as follows [32]:

$$R = UV', \text{ where SVD}(A_{DCS}A'_{RBF}) = U\Sigma V'. \tag{15}$$

The obtained translations, scaling and rotation can be combined into a singular transformation matrix, mapping DCS to RBF as follows:

$$T = T_{RBF}RsT_{DCS}, \tag{16}$$

where T is the combined transformation matrix, T_{GT} and T_{DCS} are the centroid translations of the ground truth and image frame respectively represented as 4×4-transformation matrices, R is the Procrustes rotation represented as 4×4-transformation matrix, and s is the scaling factor.

D. Path Planning

With the newly obtained mapping between DCS and RBF, the full calibration scan with markers can be placed relative to the robot. This placement allows for path planning for the Sunram 7 upon choosing a target position and orientation. An example of the breast phantom image mapped to the robot base with selected target and orientation is depicted in Fig. 5.

1) Target identification: Target identification can be done in two ways; either by manual selection of coordinates in the robot base frame or through the use of a MPR of the MRI image. The former method is trivial and useful for testing the kinematics, whilst the latter is more suitable for application in clinical settings. The MPR simultaneously presents the clinician with three linked orthogonal 2D slices reconstructed from the 3D DCS volume. This way the clinician can scroll through the volume in each direction: coronal, sagittal, and axial, and select a target based on the grayscale image of the calibration scan. This target is selected in pixels in ICS: $p_{im} = \begin{bmatrix} x_{im} & y_{im} \end{bmatrix}^T$, which is converted to DCS depending on the plane:

$$\text{yz-plane: } \begin{bmatrix} x_{DCS} \\ y_{DCS} \\ z_{DCS} \end{bmatrix} = \beta \left(\begin{bmatrix} 0 & 0 \\ 0 & 1 \\ 1 & 0 \end{bmatrix} \begin{bmatrix} x_{px} \\ y_{px} \end{bmatrix} + \begin{bmatrix} x_s \\ 0 \\ 0 \end{bmatrix} \right) \tag{17}$$

$$\text{xz-plane: } \begin{bmatrix} x_{DCS} \\ y_{DCS} \\ z_{DCS} \end{bmatrix} = \beta \left(\begin{bmatrix} 0 & 1 \\ 0 & 0 \\ 1 & 0 \end{bmatrix} \begin{bmatrix} x_{px} \\ y_{px} \end{bmatrix} + \begin{bmatrix} 0 \\ y_s \\ 0 \end{bmatrix} \right) \tag{18}$$

$$\text{xy-plane: } \begin{bmatrix} x_{DCS} \\ y_{DCS} \\ z_{DCS} \end{bmatrix} = \beta \left(\begin{bmatrix} 0 & 1 \\ 1 & 0 \\ 0 & 0 \end{bmatrix} \begin{bmatrix} x_{px} \\ y_{px} \end{bmatrix} + \begin{bmatrix} 0 \\ 0 \\ z_s \end{bmatrix} \right) \tag{19}$$

where β is the isotropic voxel size of 1.5mm and x_s, y_s, and z_s are the slice number in the respective direction. The position in DCS can be transformed to robot base using the Procrustes mapping.

2) Entrance identification: For separating the functionality between pre-operative, intra-operative and post-operative sections, the point at which the needle enters the breast must be identified. This is split up into two methodologies: an automatic and a manual selection. The latter is kept in place to keep the clinician in control of the procedure. The automatic procedure uses Algorithm 1 to minimize the distance the needle travels through the breast under the condition that the chosen point of entry must be within a voxel that can be reached at many insertion angles relative to other voxels. This condition can be tested using the IK workspace analysis discussed in Section II-B.3 by laying the thresholded voxel quality map as a mask over the workspace. The condition is required to increase the likelihood that the Sunram 7 has enough buffer to be adjusted during insertion.

Algorithm 1: Automatic Entry Point Selection

```
Data: Breast mesh vertices, Workspace mask, target
Result: Entry-point
Find vertices within voxel mask
Sort vertices based on ascending distance from target
for Sorted vertices do
    Orientation = target - vertex
    if IK(vertex, orientation) <= Joint limits then
        if IK(target, orientation) <= Joint limits then
            Entry-point found
            Break
end
```

The manual approach allows the clinican to click and drag an arrow in the RBF plotter to select the envisioned angle of insertion. From the selected orientation a line is constructed through RBF and the 25 closest vertices to this line are used to compute the entrance position as indicated in Fig. 8. The weighted average position based on the distance from the line of these 25 vertices is used to determine the entry point:

$$\mathbf{p}_e = \sum_{i=1}^{n} \frac{\frac{1}{d_i}}{\sum_{j=1}^{n} \frac{1}{d_j}} \mathbf{p}_i, \tag{20}$$

where p_e is the entry point, n is the number of closest vertices considered, d is the distance of the associated vertex to the line, and p_i is the position of the vertex. Whether

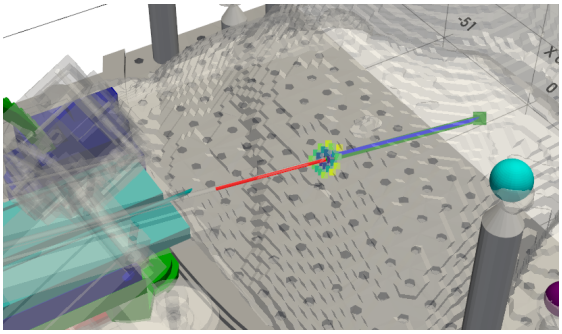

Fig. 8: Calculation of the insertion point based on the 25 closest vertices to the line along the chosen orientation. The red line is the line along the orientation and the blue line is the calculated distance through the breast tissue.

the entry point can be reached with this orientation is then determined by whether the inverse kinematics mapping obtains a joint configuration that is within the joint limits.

3) Path: The path planning of the Sunram 7 is split up into two sections; pre-operative and intra-operative. Of which the latter is discussed in Section II-F and the former based solely on the joint configuration Q at the target point and at the entry point. The pre-operative path planning is designed such that the Sunram 7 travels through the breast tissue in a straight line. Due to the kinematic design of the Sunram 7 this is as simple as moving J5 last. This also simplifies the path planning for the other joints as keeping the Sunram 7 with J5 in a retracted state circumvents any robot breast collisions. For simplicity, path planning in the XY-plane is separated from the z-direction as well, by first moving J3 and J4 to their required position. In the movement of J3 and J4 there is concern for the Sunram 7 to collide with itself for higher values of J3 when J4 is of low value. A very simple solution is proposed in first moving J4 to 10° and then performing J3 and J4 to their required position. Subsequently J1 and J4 can be moved to their respective positions. Lastly, J5 is moved directly to the entry position and the remaining distance to the target point is split into stages of 10 mm. An example of such a planned path is indicted in Table II This does not circumvent the collision for the entire workspace of the Sunram 7 but for all targets and orientations regarded relevant for the clinical implementation. Note, that the method of calibration between DCS and RBF only directly places the image with respect to the base of the robot. Thus, it is required to start the procedure with the Sunram 7 in a known zero configuration: $Q = (0, 0, 0, 0, -100)$, with respect to the base.

The planned path is discretized to steps by the discretization procedure presented hereafter in Section II-E using the stepsizes indicated in Table I. These step set-points for each consecutive joint configurations are sent to the pneumatic controller board using serial commands. The pneumatic stepper frequency of the controller board is limited to 10Hz because of the relatively long (7m) tubes for operation inside the MRI bore [22].

TABLE II: Example of a planned path for the Sunram 7 robot. Pose 4 represents the entry configuration of the Sunram 7 in the breast phantom and pose 5 at 10mm into the breast.

Pose	J1 (°)	J2 (°)	J3 (°)	J4 (°)	J5 (mm)
0	0	0	0	0	-100
1	0	0	0	10	-100
2	0	0	16.67	37.34	-100
3	-12.37	-12.49	16.67	37.34	-100
4	-12.37	-12.49	16.67	37.34	-69.46
5	-12.37	-12.49	16.67	37.34	-59.46
6	-12.37	-12.49	16.67	37.34	-49.46
7	-12.37	-12.49	16.67	37.34	-39.46
8	-12.37	-12.49	16.67	37.34	-31.58

E. Discretization error

The discrepancy between the continuous nature of the joint configuration obtained from the inverse kinematics and the discrete nature of the pneumatic stepper motors of the Sunram 7 introduce an error in reaching the target position and orientation. An obvious solution would be to round each of the joints off to the nearest step, but due to the kinematic structure of the Sunram 7, as presented in Section II-B, this might not be the ideal solution. In the context of taking biopsies, the position of the needle tip is considered most important as one must ensure to reach the lesion. Therefore, this research proposes an optimization algorithm of the discretization error based on minimizing the error of the target position whilst keeping the end-effector orientation close to the chosen orientation.

The algorithm is based on an iterative procedure of changing the joint step of the joint that has the largest component in direction of the target error, with the added caveat that already tried joint configurations cannot be tested again. Thus, on each iteration the effect of a step for each respective joint at that joint configuration is calculated:

$$\mathbf{v}_i = \mathbf{t}_{c,i+1} - \mathbf{t}_c, \tag{21}$$

where $\mathbf{v}_i$ is the effect vector of joint i, $\mathbf{t}_{i+1}$ is the end-effector position reached by adding a step to joint i at the joint configuration at that iteration, and $\mathbf{t}_c$ is the end-effector position for the joint configuration of that iteration. The component of each of the normalized joint effects along the error in end-effector position compared to the target is computed:

$$w_i = \frac{\mathbf{v}_i \cdot \mathbf{t}_e}{|\mathbf{t}_e|}, \tag{22}$$

with w the weight factor of joint i indicating its component along the error, $\mathbf{v}_i$ the effect vector of joint i, and $\mathbf{t}_e$ the error between target and end-effector position at the joint configuration. This weight vector indicates the joint that has the largest component in the direction of the target from the given joint configuration and thus should be adjusted. Note, that the sign direction of the weight indicates in what direction the joint should be adjusted.

The starting point of this algorithm are the rounded values of the exact joint steps obtained from the target position and orientation. The joint that should be adjusted is computed, it is checked whether the obtained configuration has already been tested. If not, the next iteration is started with the new joint configuration, and if it is, the joint with the second largest component is tested. If all joint adjustments are already tested, two steps in the joints from largest component in the direction of the target error is tested and so on. For each of the configurations the error, the distance between the target and the obtained end-effector position, is saved. An overview of the algorithm is presented in algorithm 2.

Algorithm 2: Discretization error optimization

```
Data: exact joint steps, target, iterations
Result: discretized joints steps
Initial joint steps: round(exact joint steps)
for iterations do
    Compute joint effects
    Compute target error for joint configuration
    Compute component joint effect along target error
    Order joints based on largest component
    for Max Steps do
        for Ordered Joints do
            if new joint configuration then
                Next iteration joint configuration
                break
        end
    end
end
```

F. Image based feedback loop

The needle has to be surrounded by tissue for it to show up on the MRI image such that it can be detected by the segmentation algorithm descibed in Z.J. Tai et al. [24]. Thus the image-based feedback loop starts from the pose in the path planning at which the Sunram 7 is inserted 10mm into the breast phantom. The segmentation algorithm starts by providing it with the estimated position of the needle entry point and tip position in PCS. The position of the end-effector at entry and for the tip position in RBF is obtained by computing the forward kinematics for the joint configurations associated with these poses. This can be converted to the DCS using the inverse of the Procrustes transformation described in section II-C.2. The Access-I API, however, uses the PCS for selecting a slice position and orientation, the mapping from DCS to PCS can be obtained from the Image Orientation (Patient) and Image Position (Patient) DICOM metadata attributes of the first slice with tags (0020, 0037) and (0020, 0032) respectively. The image orientation attribute indicates the direction of the row and column vectors of slice scanning in PCS and the image position attribute indicates the position of the top left voxel of the slice. The mapping can then be constructed as:

$$T_{PCS}^{DCS} = \begin{bmatrix} n_x & c_x & r_x & p_x \\ n_y & c_y & r_y & p_y \\ n_z & c_z & r_z & p_z \\ 0 & 0 & 0 & 1 \end{bmatrix}, \tag{23}$$

where $\mathbf{r}$ and $\mathbf{c}$ are the row and column vectors of the slice scanning direction respectively, $\mathbf{n}$ is the final orthogonal direction obtained by the cross product of $\mathbf{r}$ and $\mathbf{c}$, and $\mathbf{p}$ is the slice position of the first slice. The converted end-effector position and orientations are used to obtain the appropriate slices for the segmentation algorithm presented in Z.J. Tai et al. [24]. This algorithm returns the segmented end-effector tip and base position from this slice, which are the needle tip and the detected point of entry into the breast tissue. The needle tip position can be used as the measured end-effector tip whilst the orientation of the end-effector can be obtained by:

$$\mathbf{o}_{EE} = \mathbf{p}_{tip} - \mathbf{p}_{base}, \tag{24}$$

where $\mathbf{p}_{tip}$ is the segmented needle tip position and $\mathbf{p}_{base}$ is the segmented point of entry of the needle. These measurements can be used to update the estimated position and orientation of the end-effector, which in turn can be used to find the adjustment that needs to be made to the planned path in order to reach the target position. To prevent bending of the needle and other side-effects from needle-tissue interaction, reorientation of the end-effector is done outside of the breast phantom. Meaning that the needle is moved outside of the breast, J1-J4 are adjusted and the needle is reinserted for a new iteration of measurements.

The predicted state from the planned path and the measured state can be used to obtain the newly estimated state using Kalman filtering. Where the state for this system consists of the position and orientation: $\mathbf{x} = (p_x, p_y, p_z, o_x, o_y, o_z)$. Kalman filtering is based on the following formula for predicting the estimated state based on the prediction and measurement [33]:

$$\mathbf{x}_{k+1} = \mathbf{x}_{k+1|k} + K_k v_k, \tag{25}$$

where $\mathbf{x}_{k+1|k}$ is the predicted state at $k+1$ given the state at k, K_k is the Kalman gain, and v_k is the measurement update. This newly updated state also has a newly associated updated covariance matrix given by:

$$P_{k+1} = (I - K_k H)\, P_{k+1|k}, \tag{26}$$

where H is the measurement matrix and $P_{k+1|k}$ is the covariance prediction given the covariance at step k. For this system the predicted state $\mathbf{x}_{k+1|k}$ is taken as purely equal to the updated planned path and orientation based on the estimated state $\mathbf{x}_k$ and measurement update $\mathbf{v}_k$. The measurement update $\mathbf{v}_k$ is given by:

$$\mathbf{x}_{k+1|k} = F\mathbf{x}_k + B\mathbf{u}_k, \tag{27}$$

where in this case, to avoid mapping the kinematics into the state progression matrix, this is separated into two cases. The needle is reoriented and the process noise is reset: $F = \mathbf{0}$, $B = I$, and the control input vector: $\mathbf{u}_k = \mathbf{x}_{planned}$ after

the joints are re-calibrated to the newly estimated position based and moved back to the planned position for a new measurement. Or the needle is inserted 10mm along J5, so in the direction of the orientation vector and thus:

$$F = \begin{bmatrix} I_{3\times3} & 10 \cdot I_{3\times3} \\ 0_{3\times3} & I_{3\times3} \end{bmatrix}, \tag{28}$$

and the input vector $\mathbf{u}_k$ is zero. This predicted state given the state at k also has an associated covariance predication:

$$P_{k+1|k} = FP_kF^T + C_w, \tag{29}$$

where C_w is the process noise covariance matrix. Meaning that for reorientation the covariance matrix prediction is reset to the process noise and otherwise the correlation information between orientation and position is embedded into the covariance matrix. The measurement update $\mathbf{v}_k$ is equal to:

$$\mathbf{v}_k = \mathbf{z}_k - H\mathbf{x}_{k+1|k}, \tag{30}$$

where $\mathbf{z}_k$ is the measurement vector, $H = I$ is the measurement matrix mapping the state to the measurement space. The Kalman gain matrix at k is given by:

$$K_k = P_{k+1|k}H^T \left(HP_{k+1|k}H^T + C_v\right)^{-1}, \tag{31}$$

where C_v is the measurement noise covariance matrix. This way on each iteration the estimated state can be computed as follows:

$$\mathbf{x}_{k+1|k} = \begin{cases} x_{planned} & \text{if re-orientation} \\ F\mathbf{x}_k & \text{if insertion} \end{cases}$$

$$P_{k+1|k} = \begin{cases} C_w & \text{if re-orientation} \\ FP_kF^T + C_w & \text{if insertion} \end{cases}$$

$$\mathbf{v}_k = \mathbf{z}_k - H\mathbf{x}_{k+1|k}$$

$$K_k = P_{k+1|k}H^T \left(HP_{k+1|k}H^T + C_v\right)^{-1}$$

$$\mathbf{x}_{k+1} = x_{k+1|k} + K_k\mathbf{v}_k$$

$$P_{k+1} = (I - K_kH)\, P_{k+1|k}$$

which is basically a weighted average based on the process and measurement noise upon reinsertion and incorporates the correlation between orienation and predicted position otherwise.

Based on the newly acquired state estimation $\mathbf{x}_{k+1}$; position and orientation, on each iteration the system either retracts itself and reorients if the difference between planned and estimated is large or adjusts only slightly during insertion. Reorientation involves retraction from the breast, recalibrating to the newly estimated position and orientation, and moving to the planned trajectory for J1-J4 and inserting again along J5. Upon insertion a new iteration of the Kalman filtering is performed.

G. Experimental validations

This research is composed of a multitude of components. In order to discover the performance and accuracy of the separate components or the system as a whole the following experimental validations are set up.

1) Workpsace: A proof of concept for taking the versatility of the workspace as voxel mask for viable entry points for automatic selection of an entry point is provided by placing the voxel quality maps over a Procrustes transformed breast mesh in RBF.

2) Image processing: The main purpose of the image processing step is to accurately define the position of the six MR-visible markers in the DCS. The performance of this algorithm is tested by comparing the identified positions of the markers with the manually discovered positions of each of these markers for a set of calibration scans. Quantification of the error is done by finding the mean distance from each of the markers and the standard deviation from this error.

3) Procrustes analysis: The Procrustes analysis is used to obtain a mapping between the DCS and the RBF. The performance of the procedure is quantified by its target registration error (TRE); the distance between the mapped detected marker positions in RBF to the known ground truth. Quantification of the error is done by finding the mean distance between the transformed identified marker positions in DCS and the ground truth in combination with the standard deviation over the 15 trials.

4) Discretization error: The optimization algorithm of the discretization error is tested by comparing the obtained results with the result of simply rounding the joint configuration steps to the nearest integer and a grid search of the steps around the computed joint configuration. This comparison is done for 10 different sets of target positions and orientations. The main component of the result is the distance of the end-effector position from the target, but also the mean angle the obtained orientation has with the target orientation. The computing time needed for the algorithms also indicates the efficiency of the algorithm and the error over iterations provides insight into how many iterations would provide an acceptable error for the system.

5) Path planning: The path planning algorithm is evaluated by performing a planned path for a target position, without adjustments using the image based feedback algorithm. The planned path is compared to the segmented needle tip positions from the algorithm presented in Z. J. Tai et al. [24] and manually observed needle positions in a 3D evaluation scan after insertion. The error is quantified for both the planned path and the segmented result, by the mean perpendicular distance the points are from the line along the manually obtained needle position using the evaluation scan and the standard deviation of both methods.

6) Image-based feedback: Validation of the image-based feedback is performed by estimating the needle position during straight insertion into the breast phantom in steps of 10 mm. The segmented tip and base position obtained from the segmentation algorithm developed in Z.J. Tai et al. [24] during this insertion together with the planned path are used to estimate the needle position. To mimic both the needle advancement and reorientation with this data two different scenario's are performed whilst estimating the state using discrete Kalman filtering. The planned path is taken as the predicted state and each iteration presents a new reinsertion

along the planned path with the next segment of measurements available. Indicating the weighted average result upon reinsertion for reinsertion at one step farther along the planned path. Secondly, the needle insertion is mimicked for insertion along J5; the initial predicted value is the same as first planned path, on the second iteration the newly predicted state is taken as a 10 mm advancement into the breast from the estimated state on the previous measurement. The next iteration, the new measurement at 10mm advancement into the breast is available and the new estimate can be obtained and so on. This way the state estimation is tested by simply not adjusting the end-effector as envisioned but rather trying to improve the estimated position over purely taking the feed-forward expected position as the needle state.

III. RESULTS

The separate modules of the system are evaluated based on the empirical validations described in section II-G and the resultant metrics are presented here.

1) Workspace: The workspace analysis result for the Monte Carlo and IK methods are depicted in Figs. 9 and 10 respectively. Both workspaces are plotted as a quality map over 5100 voxels plotted in the RBF over a transformed MRI image to RBF. The colors of a voxel indicate the quality factor associated with that voxel. For the Monte Carlo method this is the normalized standard deviation of the spread in angles compared to the mean orientation for that voxel, thresholded at a value of 0.4 for opaque plotting. The yellow color indicates a high spread in angle of the obtained orientations compared to the mean orientation at that voxel, and the purple values indicate a low spread in angle at that position.

Out of the $100,000$ randomly sampled joint configurations, the end-effector position fell within the centre region defined by $\mathbf{p} = ([-40, 40], [0, 75], [20, 75])^T$ on $17,775$ occasions. This corresponds to 17.78% of the sampled positions. Given that this region constitutes 0.33 L of the total workspace volume of 4.1 L, 17.78% of the points were concentrated within 8% of the total workspace.

For the IK method the quality factor is based on the normalized amount of orientation vectors that can be reached at the position of the voxel, thresholded at a value of 0.4 for opaque plotting. A yellow color indicates a relatively large amount of orientations can be reached at that voxel position compared to others, and a purple color indicates a low amount of the orientations can be reacehed at that voxel position.

2) Image Processing: The performance of the image processing algorithm is quantified by comparing the detected MR-visible marker positions in DCS to manual selection of the marker positions. The result is presented in Table III for the target registration error over 15 trials. The marker color is correlated with the display color of the respective markers indicated in Fig. 6. The mean absolute error is indicated for each separate marker and for the combination of all markers as well as the respective standard deviations. The error in

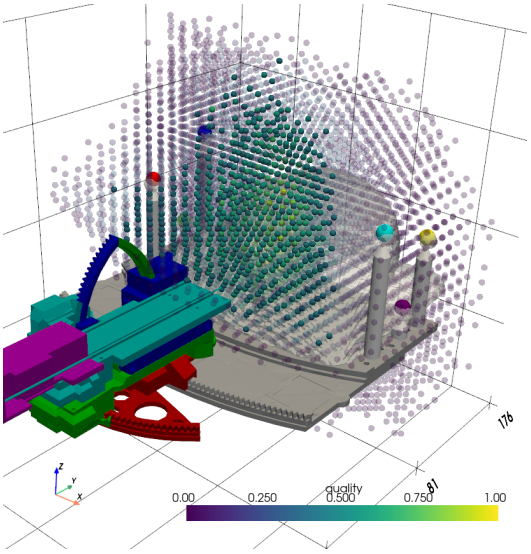

Fig. 9: The workspace of the Sunram 7 depicted using the Monte Carlo method for 100.000 randomly sampled joint configurations for a voxel size of 10×10mm. The color of the points indicates the normalized standard deviation of the insertion angles at each voxel. The threshold for plotting opaque voxels is set at a quality factor of 0.4.

position for the image processing step over all markers is 3.03 ± 0.65 mm.

Simply taking the Otsu threshold for binzarization of the 3-D calibration scan worked for 27 out of 32 total calibration scans performed. Further investigation into the remaining cases showed that simply lowering the threshold till obtaining proper marker binarization allowed for calibration with little to no impact on the obtained breast mesh. Furthermore, on the 3-D calibration scans it could be observed that the petroleum jelly based MRI visible markers are not of constant intensity throughout their volume. An indicative image of this is presented in Fig. 11, depicting the blue marker for one of the calibration scans in the trial.

Furthermore in 2 cases the template matching step found more than six markers, creating difficulties with the method of labelling the markers. Further investigation of these cases, showed that some small pieces of the phantom were disconnected from the main tissue and laid separately in the MRI bore. These tissues showed as similar lumps on the MRI-scan compared to the markers in Fig. 11.

TABLE III: The results for the image processing algorithm in segmenting the MR-visible marker positions in DCS shown in mean target registration error (Mean) and standard deviation (SD) thereof. The marker color identification matches with the respective markers in Fig. 6

	Segmented Markers					
	Red	**Green**	**Blue**	**Yellow**	**Purple**	**Cyan**
Mean (mm)	3.14	2.82	2.85	3.04	3.09	3.25
	3.03					
SD (mm)	0.66	0.66	0.74	0.62	0.60	0.58
	0.65					

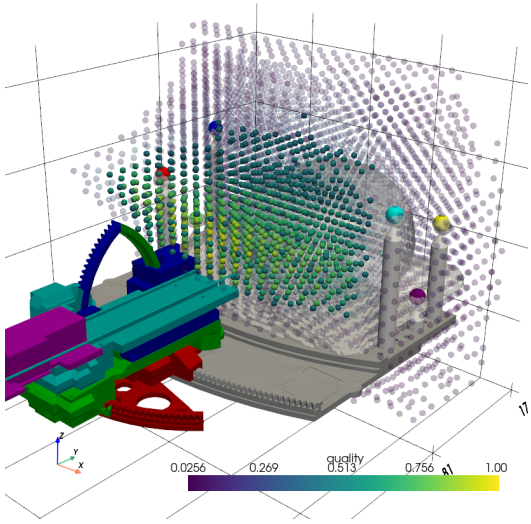

Fig. 10: The workspace of the Sunram 7 depicted using the inverse kinematics method for 100 orientation vectors at each voxel for a voxel size 10×10mm. The color of the points indicate the quality factor based on the normalized amount of orientations reachable by the Sunram 7 at each voxel. The threshold for plotting opaque voxels is set at a quality factor of 0.4.

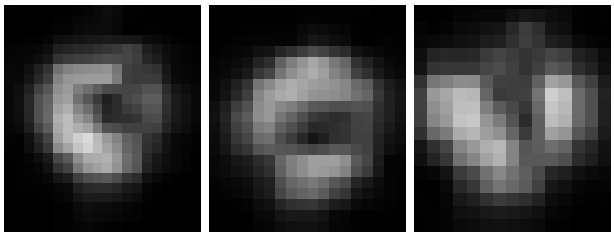

(a) Coronal (b) Sagittal (c) Axial

Fig. 11: The cross-sectional MRI image of the center of the blue marker as color coded in Fig. 6.

3) Procrustes Analysis: The result for the Procrustes analysis is presented in Table IV. The table presents the result for each marker over the columns, and the results for the separate trials in the row direction. Five trial runs are presented, but all statistical analysis is performed over all 15 available trials. The bottom right result presents the mean distance a transformed identified marker position is away from the ground truth over all markers and trials, providing an overall TRE of 0.67 ± 0.43 mm.

A one-way ANOVA test on the TRE of individual markers indicates a statistically significant difference in TRE error across colors at a 5% significance level (p = 0.0193). Further analysis using Tukey's honest significance test shows that the only significant difference is between the error of the blue and red marker with a p-value of 0.0082.

4) Discretization Error: The experimental validation for the optimization algorithm for the discretization error over ten trials is presented in Table V. The first five trials are explicitly depicted, and the statistical analysis of all ten trials is presented below these five trials. The joint effect optimization algorithm for a 1,000 iterations shows an error in target position of 0.07 ± 0.03 mm in a computation time of 5.34 ± 0.34 s. Directly rounding the steps to the nearest integer results in an error of 0.52 ± 0.25 mm in practically zero computation time, and the grid search for 100,000 iterations results in an error of 0.08 ± 0.05 mm with a computation time of 86.28 ± 1.31 s.

The amount of iterations the joint effect algorithm takes to acquire an error below 0.2 mm over the ten trials is equal to 61 ± 173 iterations. Note here, that one trial presents an outlier at iteration 580, and removing this trial from the test results in the algorithm needing 3 ± 2 iterations to realize an error below 0.2 mm. Increasing the threshold for error to 0.3 mm shows the algorithm to find a solution in 3 ± 2 iterations over all ten trials.

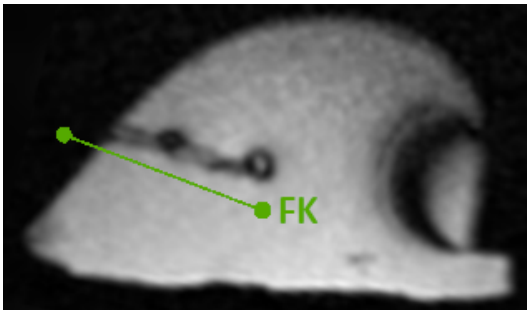

Fig. 12: The obtained 2-D slice using continuous MRI imaging from selecting the slice position and orientation in Access-I based on the FK. Showing the needle in-plane and annotated in green is the planned path of the Sunram 7 in ICS.

5) Path Planning: Fig. 13 depicts the obtained results for performing a path towards a target position in the centre of the breast. The purple line indicates the manually detected position of the needle from an evaluation scan performed with the needle tip at the planned target position. The green lines shows the planned path in robot base frame and the red line shows a least squares fitted line through the detected needle tip positions during the insertion using the algorithm disclosed in Z. J. Tai et al. [24].

The calibration scan for this trial had a mean error in transforming the marker positions in DCS to the RBF of 0.47 mm. The planned path is performed for a target position at $\begin{pmatrix} 33.47 & 94.32 & 23.93 \end{pmatrix}^T$ mm with orientation $\begin{pmatrix} -0.20 & 0.93 & -0.32 \end{pmatrix}^T$ ending up with joint configuration J1-J4= $(0.16, 0.05, 0.20, 0.52)$ rad and J5= -35.64 mm. The planned insertion path ended up with a mean orthogonal distance of 8.81 ± 1.93mm from the manually detected needle position in the evaluation scan. The needle tip segmentation algorithm during insertion obtained a mean orthogonal distance of 1.28 ± 0.61mm.

Fig. 12 shows a single slice of the continuous image obtained by providing the planned needle position and orientation in PCS to Access-I. Some imaging artefacts around the

TABLE IV: The result for the Procrustes analysis. Five trials are presented, although the statistical qualities results are depicted according to all 15 trials. The bottom row presents the error between computed marker position and ground truth (GT) across all markers (AAM) and the most right column presents the error computed marker position across all trials (AAT).

Marker	**GT** (mm)		**Trials** (mm)						**Error AAT** (mm)	**SD AAT** (mm)
			1	**2**	**3**	$\cdots$	**14**	**15**		
Red	x	-90.0	-90.59	-90.57	-90.57		-90.44	-89.36	0.70	0.42
	y	70.0	69.69	69.76	69.68	$\cdots$	69.67	69.46		
	z	65.0	63.99	64.08	64.11		64.11	64.70		
Green	x	-90.0	-89.69	-89.66	-89.52		-89.85	-89.82	0.74	0.51
	y	100.0	99.62	99.77	99.80	$\cdots$	99.75	99.70		
	z	25.0	26.59	26.35	26.27		26.51	24.38		
Blue	x	-90.0	-90.26	-90.27	-90.36		-90.31	-90.06	0.69	0.39
	y	120.0	120.64	120.45	120.43	$\cdots$	120.51	120.68		
	z	85.0	84.49	84.52	84.55		84.25	85.70		
Yellow	x	90.0	89.92	89.95	89.87		89.60	89.01	0.85	0.50
	y	120.0	119.95	120.06	119.90	$\cdots$	119.80	119.72		
	z	65.0	65.69	65.71	65.60		65.50	65.15		
Purple	x	90.0	89.78	89.97	90.05		90.43	90.58	0.52	0.32
	y	100.0	99.83	99.71	99.72	$\cdots$	99.89	100.32		
	z	25.0	24.46	24.41	24.62		24.98	24.69		
Cyan	x	90.0	90.84	90.59	90.53		90.57	89.66	0.49	0.31
	y	70.0	70.28	70.25	70.41	$\cdots$	70.37	70.12		
	z	85.0	84.78	84.93	84.85		84.65	85.37		
AAM	**Error** (mm)		0.99	0.87	0.83	$\cdots$	0.90	0.81	**0.67**	**0.43**
	SD (mm)		0.60	0.53	0.51	$\cdots$	0.56	0.48		

TABLE V: The results for the proposed joint effect algorithm (Joint) for a 1000 iterations, compared to simply rounding the steps to the nearest integer (Rounded) and a grid search algorithm (Grid) of 100000 iterations (10 per joint). Five trials are explicitly presented as an indication of specific results and the bottom row show the statistical analysis of a total of ten trials for each algorithm.

Trial	**Target**		**Algorithm**			**End-effector**		
	Pos. (mm)	**Orien.**	**Type**	**Joint Config.** (Steps)	**Iter.**	**Pos.** (mm)	**Angle** ($^\circ$)	**Error** (mm)
1	$\begin{pmatrix}25.97\\119.19\\34.65\end{pmatrix}$	$\begin{pmatrix}-0.27\\0.91\\-0.28\end{pmatrix}$	Rounded	$(80, 14, 53, 82, -3)$	n.a.	$\begin{pmatrix}26.06 & 119.49 & 35.42\end{pmatrix}^T$	0.21	0.83
			Grid	$(84, 16, 54, 84, -3)$	97676	$\begin{pmatrix}25.93 & 119.00 & 34.71\end{pmatrix}^T$	1.15	0.21
			Joint	$(77, 13, 43, 69, -9)$	931	$\begin{pmatrix}25.96 & 119.30 & 34.72\end{pmatrix}^T$	2.05	0.13
2	$\begin{pmatrix}-22.57\\94.56\\35.98\end{pmatrix}$	$\begin{pmatrix}0.03\\0.97\\-0.24\end{pmatrix}$	Rounded	$(-73, 21, 29, 53, -56)$	n.a.	$\begin{pmatrix}-22.34 & 94.36 & 36.02\end{pmatrix}^T$	0.07	0.30
			Grid	$(-72, 22, 31, 56, -55)$	66787	$\begin{pmatrix}-22.54 & 94.56 & 36.09\end{pmatrix}^T$	0.72	0.12
			Joint	$(-51, 35, 24, 45, -57)$	762	$\begin{pmatrix}-22.58 & 94.54 & 36.02\end{pmatrix}^T$	8.27	0.05
3	$\begin{pmatrix}9.9\\109.25\\55.59\end{pmatrix}$	$\begin{pmatrix}-0.07\\1.00\\-0.05\end{pmatrix}$	Rounded	$(6, 8, 34, 39, -26)$	n.a.	$\begin{pmatrix}10.10 & 109.14 & 55.62\end{pmatrix}^T$	0.02	0.23
			Grid	$(1, 6, 32, 36, -26)$	3326	$\begin{pmatrix}9.89 & 109.21 & 55.59\end{pmatrix}^T$	1.55	0.04
			Joint	$(1, 6, 36, 42, -25)$	187	$\begin{pmatrix}9.89 & 109.19 & 55.61\end{pmatrix}^T$	1.53	0.06
4	$\begin{pmatrix}46.48\\96.09\\28.33\end{pmatrix}$	$\begin{pmatrix}0.11\\0.95\\-0.30\end{pmatrix}$	Rounded	$(44, -33, 28, 58, -46)$	n.a.	$\begin{pmatrix}46.55 & 95.81 & 28.09\end{pmatrix}^T$	0.23	0.37
			Grid	$(40, -35, 31, 62, -43)$	13899	$\begin{pmatrix}46.48 & 96.09 & 28.39\end{pmatrix}^T$	1.56	0.04
			Joint	$(40, -35, 29, 59, -44)$	34	$\begin{pmatrix}46.48 & 96.03 & 28.31\end{pmatrix}^T$	1.46	0.06
5	$\begin{pmatrix}7.01\\105.01\\21.02\end{pmatrix}$	$\begin{pmatrix}-0.04\\0.97\\-0.24\end{pmatrix}$	Rounded	$(-5, 8, 8, 31, -38)$	n.a.	$\begin{pmatrix}6.97 & 105.07 & 22.01\end{pmatrix}^T$	0.40	0.99
			Grid	$(-5, 8, 8, 32, -38)$	55566	$\begin{pmatrix}6.97 & 104.97 & 20.97\end{pmatrix}^T$	0.18	0.07
			Joint	$(-3, 9, 1, 21, -39)$	345	$\begin{pmatrix}6.97 & 104.98 & 21.01\end{pmatrix}^T$	2.23	0.05
10 Trial Stat	Rounded	**Mean error** (mm)	0.52	**SD error** (mm)	0.25	**Mean computation time** (s)	0.00	**Mean Iteration**	n.a.
	Grid		0.08		0.05		86.28		57397
	Joint		**0.07**		**0.03**		**5.34**		**503**

titanium biopsy needle can be observed on the 2-D slice MRI scan. The planned path deviated from the actual path from the evaluation scan with an angle 7.48° in 3-D space, whilst the segmented needle positions deviated from the observed needle positions with an angle of 4.31°. Subsequent analysis showed that J3 did not reach its desired planned path.

The operation time for performing the planned path was 10:32 minutes. This included acquisition of the calibration scan (1:32 minutes), Procrustes analysis, target and orientation selection, obtaining joint configuration, joint effect discretization optimization algorithm, path planning, establishing TCP connection with segmentation algorithm Z.J. Tai et al. [24], robot operation and simultaneously segmenting needle tip locations.

6) Image-based feedback: The results for testing the Kalman filter for taking each iteration as a newly inserted measurement and insertion with sole calibration at the new estimated position in Figs. 14a and 14b respectively. The

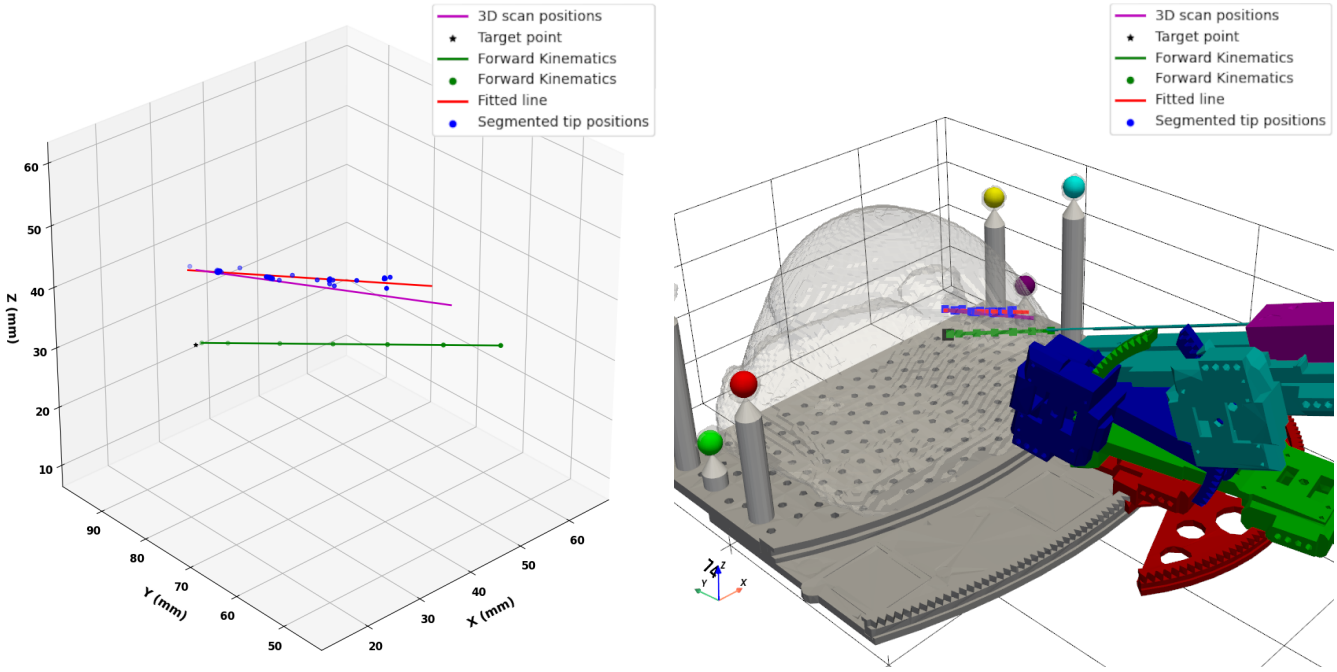

(a) Plain result

(b) Relative to the robot and breast mesh.

Fig. 13: The manually detected needle position in the evaluation MRI scan (purple) plotted against the segmented position of the needle tip in the continuous 3D tracking algorithm (red) and the planned path using the forward kinematics of the Sunram 7 (green).

estimated positions (blue) are plotted together with their respective counterparts in measurements (red) in similar shades. The measurements are the same measurements as depicted in Section III-.5 and the process and measurement noise is based on those results. Investigations of the measurements did show that the segmentation algorithm has a significant change in base position as can be seen from the measurements for iteration 3 in Fig. 14. The Kalman filter for these results was initialized with variances 10mm^2 and 0.0025 for position and orientation respectively, whilst the measurement noise variances are set at 1mm^2 and 0.05 for position and orientation respectively. The orthogonal distance and angle the estimated state makes with the needle position and orientation in the 3-D evaluation scan over the iterations for both methodologies is depicted in Table VI. The mean orthogonal distance error from the needle in the 3-D evaluation scan is 1.11mm and 1.15mm over the four iteration for reorientation and insertion methodology respectively. The mean error over the iterations in angle with the needle observed in the 3-D evaluation scan is $4.65°$ and $3.94°$ for the reorientation and insertion methodology respectively.

IV. DISCUSSION

This study proposes a methodology for closing the loop for a MRI-guided biopsy robot, presenting the envisioned procedure and required algorithms. This proposed system enables automatic path planning with continuous intra-operative imaging from selection of a target position in the MRI image by the clinician.

TABLE VI: The orthogonal distance between the estimated position and the manually observed needle position in the 3-D evaluation scan (Error) and the angle between the estimated orientation and the manually observed needle orientation in the 3-D evaluation scan (Angle) for both the reorientation and insertion validation of the Kalman filter algorithm.

		Iterations			
		1	**2**	**3**	**4**
Reorientation	**Error (mm)**	1.46	0.63	0.85	1.52
	Angle (°)	2.83	4.20	6.00	5.59
Insertion	**Error (mm)**	1.46	1.17	0.76	1.25
	Angle (°)	2.83	3.69	5.22	4.03

A. *Workspace Sunram 7*

This proposed methodology of operation of the Sunram 7 enables the option to automatically select a needle entry-position into the breast based on the Monte Carlo and IK analysis of the workspace. Both methodologies provide a quality factor of versatility of the positions in the workspace (Figs. 9 and 10). Significant overlap is shown in the voxels with a normalized quality factor higher than 0.4. The Monte Carlo method, however, has a bias towards the center of the workspace in front of the Sunram 7 in zero configuration, emphasized by the fact that 17.78% is concentrated in this region spanning only 8% of the total workspace. The influence of the bias is minimized by taking the standard deviation from the mean as the quality factor, this does not, however, remove the bias completely. The IK analysis

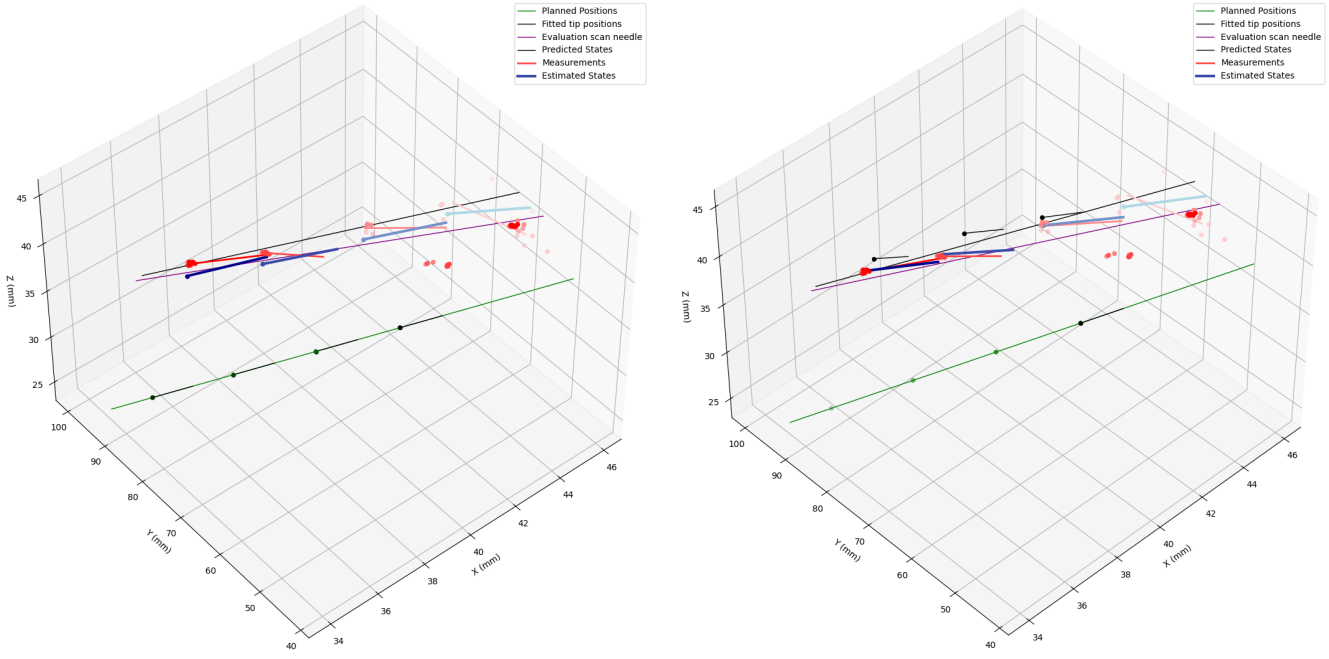

(a) Re-orientation

(b) Insertion

Fig. 14: The newly obtained state estimates using the Kalman filtering for both scenarios. The measured state (red) and the estimated state (blue) are plotted as points with an orientation line representing the needle 10mm in length. These are plotted based on iteration from a lighter to a darker shade. The predicted state (black) is plotted as a point with an orientation line 5mm in length. Additionaly the fitted needle tip position measurements are plotted, the planned path and the manually detected needle in an evaluation scan.

of the workspace provides a more equal analysis over the workspace, providing a clearer description and comparison of the versatility of the Sunram throughout the workspace. Showing the viability of taking the closest breast entry vertex to the target point within a voxel with a quality factor above a certain threshold (0.4). This methodology does not take into account the angle of insertion or the target position when computing the versatility factor. This could mean that even though the Sunram 7 can reach multiple insertion angles at this entry-point, the required orientation might be at the edge of the viable options limiting the possible corrections during the intra-operative procedure. Leaving out the target position and target orientation on the other hand does allow for precomputing the workspace analysis and loading it independent of lesion site during execution, thereby saving overall operation time.

B. Image Processing

The mean error in identification of the marker positions in DCS is equal to twice the isotropic voxel length at 3.03 ± 0.65 mm. The centroid of the template matched connected voxels at the marker position is thus shifted by two voxels compared to the actual position. This error is rather large considering the diameter of the markers of 10 mm and can be attributed to different factors that can be improved upon. Firstly, the manual selection of the centre of the markers was limited to single voxels, so the minimum step was 1.5 mm for these values, whilst the exact true marker position might be in between voxel positions. Secondly, the petroleum based markers show significant difference in intensity on the calibration scan as indicated in Fig. 11, whilst the template matching algorithm relies on the theoretically spherical marker identification. Optimizing the shape for a template matching algorithm such that it separates it from the main breast and shows a clearer indication of its position or implementing passive micro-coil fiducial markers for this purpose [34].

Furthermore, using Otsu threshold to binarize the image worked for 25 out of 30 calibration scans. The five remaining cases could be resolved by simply taking a lower threshold value without visible effect on the breast mesh, therefore showing only little delay in procedure. The two scans for which more than six markers were identified were completely fixed once the debris of breast phantom were removed from the MRI-scan. Using a more distinctive fiducial marker is also expected to minimize this problem in identification.

Lastly, a simplifying the calibration system could be done by using MRI-identifiable markers that show up with a different intensity compared to the breast/breast phantom to possibly remove the need for template matching by using Otsu multithresholding [29]. Thereby next to separating the background from the tissue, also separating the markers 'tissue' from breast tissue directly based on the different peaks of intensity with which these show up.

C. Procrustes Analysis

The Procrustes calibration results in Table IV show a total TRE of 0.67 ± 0.41 mm. This TRE is similar to the result obtained in L. Marx et al. [28] at 0.86 ± 0.35 mm, which formed the basis for the adapted version presented here. Considering the results of the image processing step, however, this result does not provide a complete picture as the Procrustes analysis performs translation, scaling and rotation to match the detected marker positions with a certain error to the ground truth positions. Thereby, certain consequent errors in detected marker positions can be masked due to the Procrustes analysis, e.g. due to uneven maker intensity as depicted in Fig. 11. This is underlined by the fact that there can be deemed a significance difference in the error over the 15 trials between the blue and red marker with a confidence level of 5%. Subsequent analysis on the bias in the error in a certain direction in the image processing step could provide insight in the difference in error for the cyan and yellow marker in the Procrustes analysis. General improvement of the marker identification can improve the entire calibration overall as the Procrustes analysis has a significantly lower error.

D. Discretization Error

From the discretization results, depicted in Table V, one can see that the error in the target position is a lot lower over ten trials when using the 'joint effect' algorithm compared to simply rounding the steps at a respective error of 0.07 ± 0.03 mm and 0.52 ± 0.25 mm. Note, however, that this can come at a cost in terms of the end-effector orientation compared to the selected orientation. With the context of taking breast biopsies, for this paper the error in target position is deemed more important for the simple requirement of reaching the lesion site. Even if firm restrictions on angle of approach are present, the algorithm can easily be extended in this regard with restrictions on the new configurations that can be tested by the angle these would make with the selected orientation.

Furthermore, the 'joint-effect' algorithm shows to be able to generally reach a better result over ten trials than the grid search algorithm in significantly less time at an error of 0.07 ± 0.03 mm in 5.34 ± 0.34 s and 0.08 ± 0.05 mm in 86.28 ± 1.31 s respectively. Again, the angle of insertion strays further from the selected, but this is to be expected based on the kinematics: as sets of steps further from the 'non-discretized' steps are directed at the same target point. The improved error and the shorter amount of time over these ten trials emphasizes the efficient way that the algorithm 'looks' through the available joint configurations. The third and fourth trial in Table V show that the 'joint-effect' algorithm does not always find a better result in $1,000$ iterations compared to the grid search of $100,000$ iterations, indicating that the algorithm suffers somewhat from local minima's. This could be addressed by looking into possible methods to move away from these local minima's, like random restarts [35], adaptive restarts [36], particle swarm optimization [37], or using knowledge of the continuous joint configuration to intelligently move around the joint configuration space. The fact that over the ten trials the 'joint effect' algorithm was able to reach an error below 0.3 mm in 3 ± 2 iterations over the ten trials shows promise for these methodologies to be able to cut-down on computation time even more whilst possible lowering the error.

In short, the methodology is proven in terms of minimizing the discretization error at the target position for the Sunram 7 and is versatile in adaptation for implementing other constraints whilst keeping computation time acceptable. Especially, seeing that it only has to be ran once after selecting the target and orientation. If computation time would be of greater importance, the algorithm shows to find an considerable improvement over directly rounding of the errors by finding an error below 0.2 mm within 3 ± 2 iterations, with the notable exception of outlier trial 1. Increasing the threshold for the error to 0.3 mm the expected amount of iterations is 3 ± 2 over all ten trials indicating its benefit over simply rounding the values directly at very low computation times under 0.05 s. However, as the ten trials is a rather small sample size, a greater trial size should help define the exact accuracy of this procedure. Its benefit over simply rounding the steps to the nearest integers and the grid search algorithm are already proven here.

E. Path Planning

The planned path had a rather large difference with respect to the observed path with a mean orthogonal distance of 8.81 ± 1.93mm. This error is largely present in the z-direction, even showing to have a combination in calibration and navigation causing difference of about six steps for J4. Comparing this to the reported accuracy (euclidian distance form a target) of the Sunram 7 in free air in H. Ranjan et al. [22] of 2.54 ± 0.86 mm and in L. Marx et al. [28] 1.36 ± 0.89 mm shows that this is a rather large error. Whilst this paper mainly focuses on closing the loop to be able to deal with the this error and compensate for it, it is acknowledged that any combination of the following factors could be a possible cause for the rather large error. Calibrating the Sunram 7 to its zero-configuration can cause any of the joints in the robot to be in between successive steps [22]. Causing the robot to not generally start in the same or optimal position causing a successive error in the path planning as the zero configuration is assumed to be perfect. Next to this, it was observed that what was considered to be the zero-configuration of J4 practically means that end-effector is three steps lower due to gravity and needle-tissue interaction. The mapping of the target position to the RBF is dependent on the calibration error of the system. Upon insertion, the needle experiences forces when moving through the tissue, this can cause possible bending in both the needle or the base frame causing further displacement of the needle compared to the planned path. Luckily, the needle segmentation algorithm is shown to have a mean orthogonal distance from the observed needle of 1.28 ± 0.61mm and considering average lesion size ranging from 3 mm to 70 mm, the test does show promise that the continuous image feedback can prove its worth in assisting with MR-guided breast biopsies.

F. Image-based feedback

The result depicted in Section III-.6 serves as a proof-of-concept for the proposed image-feedback algorithm to improve the accuracy of the Sunram 7 in performing breast biopsies. The algorithm still requires testing in several different scenarios for a definitive analysis, especially one in which the estimated position is used to re-calibrate the robot joint-configuration for new measurements, but the obtained result shows significant decrease in the mean orthogonal distance between actual needle position from the pure feed-forward part at 8.81 mm to 1.11 mm. This shows the possibility of using the measurement data in combination with the planned path to optimize the estimation of the end-effector position and orientation. This is emphasized by the relatively large feed-forward error compared to associated researches of L. Marx et al. [28] and H. Ranjan et al. [22] addressed in section IV-E. Especially, noticing that a several of the discussed causes can be linked to an issue with calibration and subsequent movement after re-calibration should decrease this uncertainty. Further measurements of the system can be used to further enhance the Kalman filtering in optimizing the variances for the process noise and measurement noise as well as selecting a smart choice of state progression matrix. For example, incorporating the prior-knowledge that the first insertion of the needle is with a larger uncertainty due to calibration errors compared to a second insertion with a significantly amount of steps performed in the joint configuration can largely improve the estimation. Investigation of the measurements highlighted that the segmentation identified a change in detected base of the needle, this is not to be expected for a straight insertion as was performed for these measurements. Therefore, it might be possible to look into an algorithm that removes outliers from the mean base position for further analysis, as this hugely influences the measured orientation.

Note that adjustments of the needle whilst inside tissue led to significant bending of the needle and should be avoided when reorienting the robot. Therefore, as the current segmentation method of the needle requires it to be surrounded by tissue the needle should be retracted, reoriented and reinserted for the next iteration of measurements. Only small changes in steps can be made whilst the needle is inside the breast phantom, with the range of possible adjustments decreasing as the needle is inserted deeper. Placing MRI-visible fiducial markers that do not require surrounding tissue along the end-effector at known locations would allow for orienting the end-effector before insertion. The proposed algorithm can still be used to obtain the initially required slice to get the fiducials in frame, and subsequent segmentation of these fiducials would allow for re-calibration of the joints and subsequent adjustment of the path as described in this paper. Removing the need for insertion to provide feedback to the robot, allowing for large adjustment to be made before insertion, which would otherwise result in unnecessary tissue damage for the patients.

Further improvements can be related to include lesion segmentation during insertion and thereby also providing information on the lesion position, possibly dealing with movement of the lesion due to deformation and compression of the breast.

G. Comparison with state-of-the-art MRI guided biopsy robots

This paper provides a proof of concept for the envisioned MR-image based feedback for the Sunram 7 robot. The envisioned feedback protocol is compared with state-of-the-art MRI guided biospy robots specifically in regards to this methodology.

The robot presented in B. Yang et al. [13] is based on a tele-operated primary-secondary robot principle which follows a similar technique to provide MR-image based feedback. Similarly, high resolution anatomical images are used to identify a target location and a point of insertion. Initial positioning of the robot is done using an MR visible marker attached to the needle holder and aligning that with the entry point and target position. The clinician is then provided with dynamic imaging (rapid gradient echo sequence) at 2.5 frames per second in the planned plane of traversal for tracking the insertion. Next to this, the clinician is also provided with both force-feedback interface; depicting the force along the needle axis measured with a MRI-compatible fiber-optic force sensor. During the seven performed ex vivo trials to robot comes within $2-4$mm of the target location six times and in one trial the target is missed by about 8mm. Although the imaging methodology does have a lot of overlap, this system has a very distinct differences to the system proposed here: the imaging is only used for visual feedback to the clinician in controlling the master robot and no segmentation is performed to obtain the position of the needle in order to close the loop on the control algorithm. Comparing the presented ex vivo results of the system in B. Yang et al. [13] ranging from $2-8$ mm of the target location with the proof-of-concept here moving within 1.15 ± 0.26 mm shows promise in improving on this accuracy.

The dedicated breast support device presented in C. Song et al. [14] uses a single calibration scan to intialize the system. Further control is based on this scan and reconstruction of the biopsy needle in the 3D scan based on control using a stero-camera setup to position the guiding cannula. Then the insertion is performed whilst the system provides image feedback to the clinician by reconstruction of the biopsy needle in the 3-D calibration scan based on the stereo-camera setup. Showing an ex vivo puncture error of 1.04 ± 0.15 mm. This system, however, only provides image feedback from a reconstruction based on an MRI scan that was performed before having to move the patient out of the MRI bore for operation of the robot and needle insertion, thereby a greater error can be expected in vivo as movement of the patient will play a role. This methodology currently cannot provide feedback through intra-operative imaging of the system.

The soft pneumatic biopsy robot SoNIM presented in J. Cheng et al. [15] closes the loop using a motion control system to provide feedback on the needle tip. Similar to

the Sunram 7, the SoNIM soft actuator has the benefit of having relatively low production costs. It also demonstrates the possibility of using MR imaging to close the loop, but does not present any closed control loop as such. Using the motion control system the target accuracy was equal to 2.9 ± 0.98 mm, but thereby lacking any possible intra-operative imaging of the needle-lesion relation.

V. CONCLUSION

A novel methodology was developed to enable closed-loop control of the Sunram 7 pneumatic MRI-safe MRI biopsy robot in order to enable continuous intra-operative imaging of the system for possible improvement of the targeting accuracy. This approach utilizes six MRI-visible markers to achieve calibration between DICOM image frame and the robot base frame, facilitating path planned based on a selected target and insertion angle. Based on the planned path and bi-directional communication with the MRI-scanner continuous 2-D MR imaging in-plane of the end-effector is achieved. Segmented tip and base positions of the end-effector in combination with the planned path are used to estimate the end-effector position and orientation in order to re-calibrate the joint-configuration of the robot throughout the procedure. Proof-of-concept results demonstrates a significant reduction in the error of the feed-forward estimated position, from 8.813mm to 1.11mm, indicating the potential of the system for enhanced accuracy. The completion of the feed-forward path in 10 minutes and 32 seconds further suggests a reduction in overall operation time. Additional functionalities, such as multi-planar reconstruction (MPR) for target selection, automatic entry-point, path planning, and discretization optimiztation, were successfully integrated. Future work should focus on extensive testing while dynamically updating the robot's path using the proposed closed-loop and optimizing Kalman filter variables. Additionally, several identified issues should be addressed to improve the feed-forward performance of the system.

APPENDIX

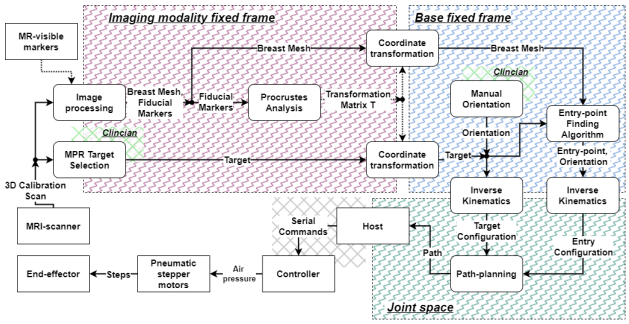

Fig. 15: Schematics of the pre-operative phase of the system.

ACKNOWLEDGMENT

First and foremost, I would like to thank Dr. Kenan Niu and Dr. Vincent Groenhuis for their supervision throughout my thesis. I enjoyed the discussions on the topics and their continuous insights. The experience of working on such a large project with contributions from many people over the years provided an amazing learning oppertunity. I would also like to thank Dr. Wyger Brink for all things related to the MRI scanner as well as Jaap Greve and Remco Liefers for supervision when using the MRI scanner. Finally, I would like to thank all committee members: Dr. Kenan Niu, Dr. Vincent Groenhuis, Dr. Janset Dasdemir, and Prof. Dr. Stefano Stramigioli for provinding me with the oppertunity.

REFERENCES

[1] F. Bray, M. Laversanne, H. Sung, J. Ferlay, R. L. Siegel, I. Soerjomataram, and A. Jemal, "Global cancer statistics 2022: Globocan estimates of incidence and mortality worldwide for 36 cancers in 185 countries," *CA: A Cancer Journal for Clinicians*, vol. 74, no. 3, pp. 229–263, 2024. [Online]. Available: https://acsjournals.onlinelibrary.wiley.com/doi/abs/10.3322/caac.21834

[2] J. Ferlay, M. Ervik, F. Lam, M. Laversanne, M. Colombet, L. Mery, M. Piñeros, A. Znaor, I. Soerjomataram, and F. Bray. (2024) Global Cancer Observatory: Cancer Today. Lyon, France: International Agency for Research on Cancer. [Online]. Available: https://gco.iarc.who.int/today,accessed[24092024]

[3] F. Sardanelli and F. Podo, "Breast MR imaging in women at high-risk of breast cancer. Is something changing in early breast cancer detection?" *European Radiology*, vol. 17, no. 4, pp. 873–887, 04 2007. [Online]. Available: https://doi.org/10.1007/s00330-006-0389-9

[4] S. C. Houghton and S. E. Hankinson, "Cancer Progress and Priorities: Breast Cancer," *Cancer Epidemiology, Biomarkers & Prevention*, vol. 30, no. 5, pp. 822–844, 05 2021. [Online]. Available: https://doi.org/10.1158/1055-9965.EPI-20-1193

[5] T. B. Bevers, B. O. Anderson, E. Bonaccio, S. Buys, M. B. Daly, P. J. Dempsey, W. B. Farrar, I. Fleming, J. E. Garber, R. E. Harris, A. S. Heerdt, M. Helvie, J. G. Huff, N. Khakpour, S. A. Khan, H. Krontiras, G. Lyman, E. Rafferty, S. Shaw, M. L. Smith, T. N. Tsangaris, C. Williams, and T. Yankeelov, "Breast cancer screening and diagnosis," *Journal of the National Comprehensive Cancer Network J Natl Compr Canc Netw*, vol. 7, no. 10, pp. 1060 – 1096, 2009. [Online]. Available: https://jnccn.org/view/journals/jnccn/7/10/article-p1060.xml

[6] W. Ren, M. Chen, Y. Qiao, and F. Zhao, "Global guidelines for breast cancer screening: A systematic review," *The Breast*, vol. 64, pp. 85–99, 2022. [Online]. Available: https://www.sciencedirect.com/science/article/pii/S0960977622000765

[7] V. Papalouka, F. Kilburn-Toppin, M. Gaskarth, and F. Gilbert, "Mri-guided breast biopsy: a review of technique, indications, and radiological–pathological correlations," *Clinical Radiology*, vol. 73, no. 10, pp. 908.e17–908.e25, 2018. [Online]. Available: https://www.sciencedirect.com/science/article/pii/S0009926018302228

[8] Z. He, Z. Chen, M. Tan, S. Elingarami, Y. Liu, T. Li, Y. Deng, N. He, S. Li, J. Fu, and W. Li, "A review on methods for diagnosis of breast cancer cells and tissues," *Cell Proliferation*, vol. 53, 06 2020.

[9] C. Riedl, N. Luft, C. Bernhart, M. Weber, M. Bernathova, M.-K. Tea, M. Rudas, C. Singer, and T. Helbich, "Triple-modality screening trial for familial breast cancer underlines the importance of magnetic resonance imaging and questions the role of mammography and ultrasound regardless of patient mutation status, age, and breast density," *Journal of clinical oncology : official journal of the American Society of Clinical Oncology*, vol. 33, 02 2015.

[10] M.-C. Chevrier, J. David, M. E. Khoury, L. Lalonde, M. Labelle, and I. Trop, "Breast biopsies under magnetic resonance imaging guidance: Challenges of an essential but imperfect technique," *Current Problems in Diagnostic Radiology*, vol. 45, no. 3, pp. 193–204, 2016. [Online]. Available: https://www.sciencedirect.com/science/article/pii/S036301881500105X

[11] H. Abe, R. A. Schmidt, R. N. Shah, A. Shimauchi, K. Kulkarni, C. A. Sennett, and G. M. Newstead, "Mr-directed ("second-look") ultrasound examination for breast lesions detected initially on mri: Mr and sonographic findings," *American Journal of Roentgenology*, vol. 194, no. 2, pp. 370–377, 2010.

[12] M. L. Huang, M. Speer, B. E. Dogan, G. M. Rauch, R. P. Candelaria, B. E. Adrada, K. R. Hess, and W. T. Yang, "Imaging-concordant benign mri-guided vacuum-assisted breast biopsy may not warrant mri follow-up," *American Journal of Roentgenology*, vol. 208, no. 4, pp. 916–922, 2017, pMID: 28140609. [Online]. Available: https://doi.org/10.2214/AJR.16.16576

[13] B. Yang, S. Roys, U.-X. Tan, M. Philip, H. Richard, R. P. Gullapalli, and J. P. Desai, "Design, development, and evaluation of a master–slave surgical system for breast biopsy under continuous mri," *The International journal of robotics research*, vol. 33, no. 4, pp. 616–630, 2014.

[14] C. Song, Z. Yang, S. Jiang, Z. Zhou, and D. Zhang, "An integrated navigation system based on a dedicated breast support device for mri-guided breast biopsy," *International Journal of Computer Assisted Radiology and Surgery*, vol. 17, no. 6, pp. 993–1005, 2022.

[15] J. Chen, J. Zhang, T. Jiang, Y. Dang, and J. Han, "Design and analysis of an mri-compatible soft needle manipulator," in *Actuators*, vol. 13, no. 2. MDPI, 2024, p. 59.

[16] M. Anvari, T. Chapman, K. Barlow, T. Cookson, C. Van Toen, and T. Fielding, "Clinical safety and efficacy of a fully automated robot for magnetic resonance imaging-guided breast biopsy," *The International Journal of Medical Robotics and Computer Assisted Surgery*, vol. 19, no. 2, p. e2472, 2023.

[17] D. Stoianovici, C. Kim, D. Petrisor, C. Jun, S. Lim, M. W. Ball, A. Ross, K. J. Macura, and M. Allaf, "Mr safe robot, fda clearance, safety and feasibility prostate biopsy clinical trial," *IEEE/ASME transactions on mechatronics : a joint publication of the IEEE Industrial Electronics Society and the ASME Dynamic Systems and Control Division*, vol. 22, no. 1, p. 115—126, February 2017.

[18] H.-L. Park and J. Hong, "Vacuum-assisted breast biopsy for breast cancer," *Gland surgery*, vol. 3, no. 2, p. 120, 2014.

[19] D. M. Pinkney, S. A. Chikarmane, and C. S. Giess, "Do benign-concordant breast mri biopsy results require short interval follow-up imaging? report of longitudinal study and review of the literature," *Clinical Imaging*, vol. 57, pp. 50–55, 2019. [Online]. Available: https://www.sciencedirect.com/science/article/pii/S0899707119300956

[20] F. W. Hirsch, J. Frahm, I. Sorge, C. Roth, D. Voit, and D. Gräfe, "Real-time magnetic resonance imaging in pediatric radiology—new approach to movement and moving children," *Pediatric Radiology*, vol. 51, pp. 840–846, 2021.

[21] F. J. Siepel, B. Maris, M. K. Welleweerd, V. Groenhuis, P. Fiorini, and S. Stramigioli, "Needle and biopsy robots: A review," *Current Robotics Reports*, vol. 2, pp. 73–84, 2021.

[22] H. Ranjan, M. Van Hilten, V. Groenhuis, J. Verde, A. Garcia, S. Perretta, J. Veltman, F. J. Siepel, and S. Stramigioli, "Sunram 7: An mr safe robotic system for breast biopsy," in *2023 IEEE/RSJ International Conference on Intelligent Robots and Systems (IROS)*. IEEE, 2023, pp. 10 281–10 288.

[23] J. C. Gower, "Procrustes methods," *Wiley Interdisciplinary Reviews: Computational Statistics*, vol. 2, no. 4, pp. 503–508, 2010.

[24] Z. J. Tai, V. Groenhuis, W. Brink, S. Stramigioli, and K. Niu, "Real-time mri-guided needle tracking for interventional procedures," MSc Thesis, University of Twente, Enschede, the Netherlands, Oct 2024.

[25] V. Groenhuis, "Sunram 7 technical document," Enschede, the Netherlands, Oct 2023.

[26] R. M. Murray, Z. Li, and S. S. Sastry, *A mathematical introduction to robotic manipulation*. CRC press, 2017.

[27] J. Rastegar and B. Fardanesh, "Manipulation workspace analysis using the monte carlo method," *Mechanism and Machine Theory*, vol. 25, no. 2, pp. 233–239, 1990.

[28] L. Marx, S. Stramigioli, K. Niu, V. Groenhuis, and W. Brink, "Augmented reality based digital twin to control mri compatible robot," MSc Thesis, University of Twente, Enschede, the Netherlands, Jan 2024.

[29] N. Otsu *et al.*, "A threshold selection method from gray-level histograms," *Automatica*, vol. 11, no. 285-296, pp. 23–27, 1975.

[30] G. S. Cox, "Template matching and measures of match in image processing," *University of Cape Town, South Africa*, 1995.

[31] S. H. Friedberg, A. J. Insel, and L. E. Spence, *Linear Algebra: Pearson New International Edition*, 4th ed. Pearson Higher Ed, 2014.

[32] K. V. Mardia, J. T. Kent, and J. M. Bibby, *Multivariate Analysis*, 4th ed. ACADEMIC PRESS, Harcourt Brace & Company, 1995.

[33] F. Van Der Heijden, R. P. Duin, D. De Ridder, and D. M. Tax, *Clas-*

sification, parameter estimation and state estimation: an engineering approach using MATLAB. John Wiley & Sons, 2005.

[34] M. Rea, D. McRobbie, H. Elhawary, Z. T. Tse, M. Lamperth, and I. Young, "Sub-pixel localisation of passive micro-coil fiducial markers in interventional mri," *Magnetic Resonance Materials in Physics, Biology and Medicine*, vol. 22, pp. 71–76, 2009.

[35] X. Hu, R. Shonkwiler, and M. C. Spruill, "Random restarts in global optimization," *Georgia Institute of technology, Atlanta*, 1994.

[36] L. Mathesen, G. Pedrielli, S. H. Ng, and Z. B. Zabinsky, "Stochastic optimization with adaptive restart: A framework for integrated local and global learning," *Journal of Global Optimization*, vol. 79, pp. 87–110, 2021.

[37] J. Kennedy and R. Eberhart, "Particle swarm optimization," in *Proceedings of ICNN'95-international conference on neural networks*, vol. 4. ieee, 1995, pp. 1942–1948.